

Theory and Application of Synthetic Seismograms.

D. V. HELMBERGER

Seismological Laboratory, 252-21, California Institute of Technology - Pasadena, Cal. 91125

1. - Introduction.

In the past decade, our understanding of earthquakes and Earth structure has increased significantly based on our improved ability to interpret seismograms. Numerous formalisms have been developed whereby synthetic seismograms can be computed at positions on the Earth for comparisons with observed seismograms. The various processes that affect the motion at some field point such as the seismic source, Earth model response, attenuation and recording equipment, are all combined into the synthetic convolution operators. Since these effects can be treated as linear operators to first order, it becomes simple to test the significance of changes in the synthetics caused by varying the operators separately. By comparing the synthetic with observed seismograms we can apply iterative techniques to determine Earth structure or source model, or perhaps some properties of each depending on the circumstances. Applications of this procedure to body waves have proven quite effective in determining the source properties of shallow earthquakes. We shall review these studies in some detail in this set of notes.

There are four basic operators which are generally included in the generation of synthetics. These represent the seismic instrumental response, $I(t)$, the attenuation operator, $A(t)$, the source operator, $S(t)$, and a wave propagation operator or Green's function, $M(t)$. The synthetic seismogram, $SS(t)$, is computed by the triple convolution

$$SS(t) = I(t) * A(t) * M(t) * S(t),$$

where only the first of these is generally well known.

We will be primarily interested in events recorded by the World-Wide Seismic System Network (WWSSN). This global network of stations is displayed in fig. 1.1. Each station records three components of motion, namely vertical, North-South and East-West, on photographic paper. Because the Earth is particularly noisy at about 4 s, it is convenient to record each component

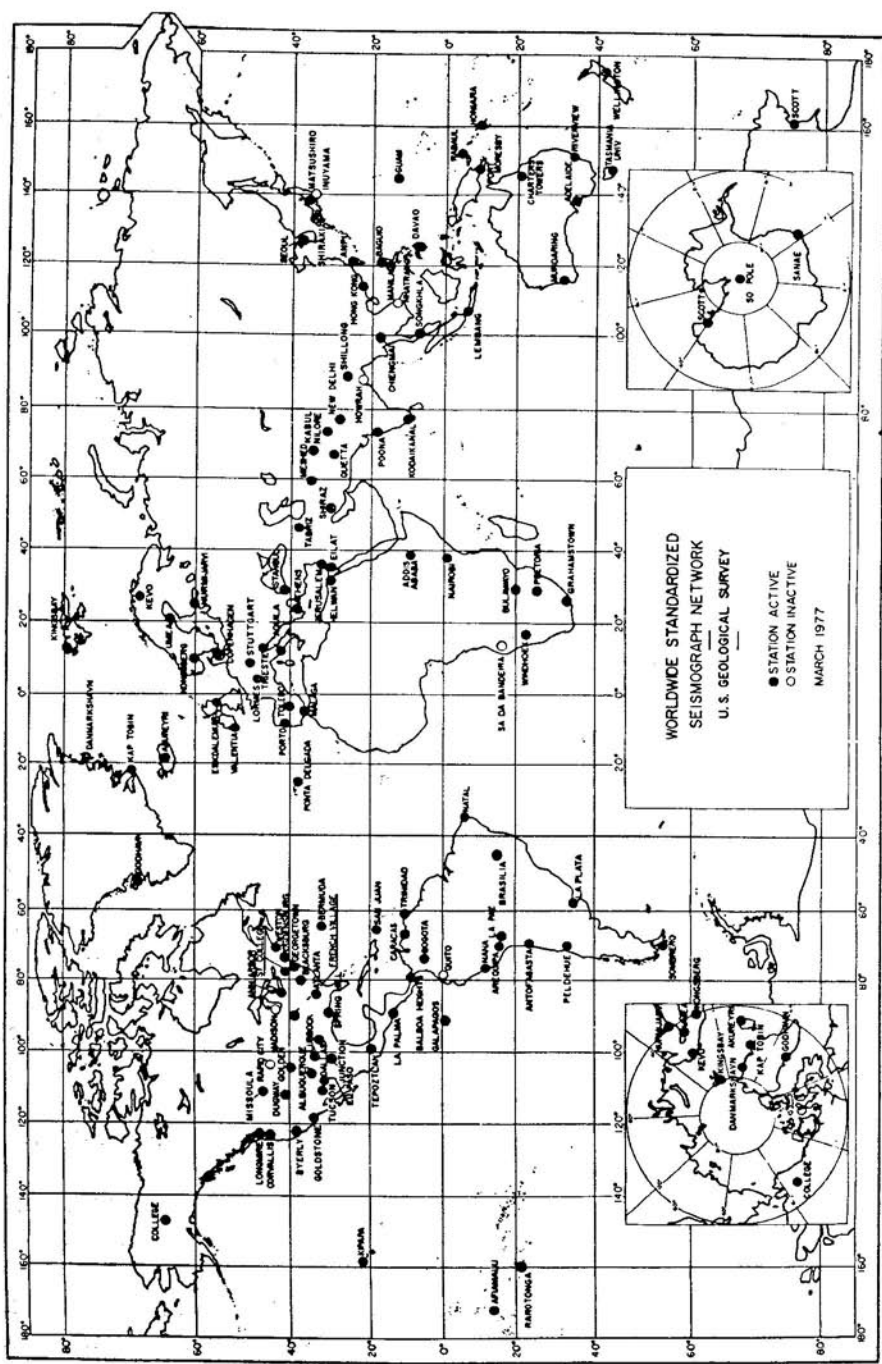


Fig. 1.1. - WWSS global network (after USGS).

in two pass-bands, short period (SP) and long period (LP). The gains or amplifications of SP's are normally between 25 to 200 thousand, while the LP's run at 750 to 3000.

The attenuation operator does not introduce any structure into the wave forms in most problems of interest, but only smooths the results. The operator which is most commonly used could be more properly written $A(r, t^*)$, where $t^* = \int ds/Q$, where Q is the quality factor and the integration is performed along the path of the ray (see [1, 2]). Most recent estimates of t^* are near 1 for P -waves and 4 or larger for shear waves assuming shallow events. The effects of the attenuation operator convolved with the instrumental responses are displayed in fig. 1.2. Note that for a t^* of 4 the short periods are greatly

synthetic
observe

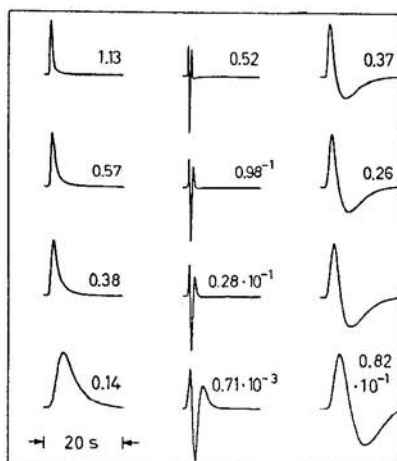


Fig. 1.2. — The first column displays $A(t, t^*)$ as a function of t^* assuming 0.5, 1.0, 1.5 and 4, from top to bottom. The middle column displays the convolution of $A(t, t^*)$ with the short-period instrumental response, and similarly for the long-period on the right. The relative amplitudes are indicated by the numbers above each trace.

reduced. Thus we should not expect to see short-period shear waves from shallow sources, which is generally true. There is considerable evidence for a frequency-dependent attenuation operator, particularly at the high frequencies (say > 3 Hz) (see [3]). We will be primarily interested in the long-period seismograms and will apply the $A(t^*, t)$ for simplicity.

Calculating $M(t)$ can be quite simple or complex depending on circumstances and epicentral distances. At teleseismic distances, 30° to 90° , we can assume that $M(t)$ is a delta-function and the only remaining complexity is due to surface reflections (see fig. 1.3). From about 12° to 30° , the Earth's upper-mantle triplications introduce additional frequency-dependent arrivals making $M(t)$ more interesting. At smaller ranges, the crust plays a more important role and the guided waves following the P -wave prove quite useful. Methods for gen-

Fig. 1.3. — Examples of $M(t)$ for simple ($> 30^\circ$), slightly complicated (less than $= 337^\circ$; b) upper mantle, Oroville, 8.1.1975, A

erating $M(t)$ abound in the recent text theory, GRT, and are familiar with this

2. — Source description

The seismic radiation can be generated in several means. In the initial stress and analytical or numerical methods (for example, [4]). Anomalous source mechanisms called the shear-wave splitting attempt to understand the seismic zone, but simply as dislocation.

However, before we consider the shear dislocation, let us consider the symmetrically symmetric

2.1. Symmetric
lindrical co-ordinates prove advantage will, also, take into account will prove useful

gains or am-
hile the LP's

nto the wave
lts. The op-
itten $A(r, t^*)$,
is performed
 t^* are near 1
events. The
ital responses
ls are greatly

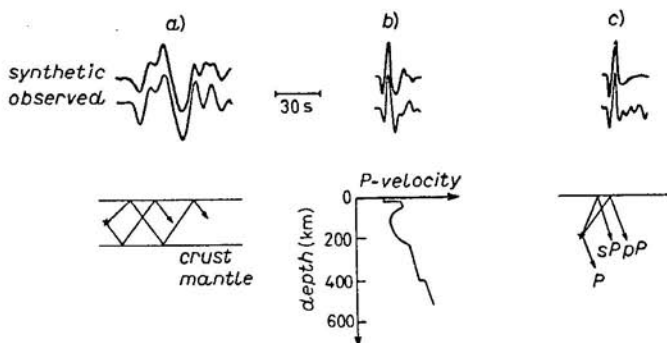


Fig. 1.3. - Example observations and synthetics at ranges where the Earth appears simple ($> 30^\circ$), slightly complicated (upper-mantle ranges, 30° to 14°) and quite complicated (less than 14°): a) regional, Truckee, 9.12.1966, COR, $\Delta = 6.0^\circ$, azimuth = $= 337^\circ$; b) upper mantle, Oroville, 8.1.1975, FFC, $\Delta = 20.9^\circ$, azimuth = 34° ; c) $> 30^\circ$, Oroville, 8.1.1975, ARE, $\Delta = 73^\circ$, azimuth = 130° .

erating $M(t)$ abound and their descriptions are covered in great detail in any of the recent textbooks. In this set of notes, we will apply generalized ray theory, GRT, and the Cagniard-de Hoop formalism, since the author is the most familiar with this technique and it can be used effectively at all ranges.

2. - Source descriptions and generalized ray theory.

The seismic radiation field produced by earthquakes can be represented by several means. Following the stress relaxation approach, one assumes the initial stress and frictional conditions and performs the proper dynamics using analytical or numerical techniques to obtain the displacements (see, for example, [4]). Another particularly useful approach is due to HASKELL [5], called the shear-dislocation model. Following this approach one does not attempt to understand the detailed mechanics involved in the actual fault zone, but simply states that slip occurs on a specified surface, referred to as a dislocation.

However, before getting into the substantial complexities involved in the shear dislocation formalism, it appears useful to review a much simpler spherically symmetric source or an idealized point source explosion.

2.1. Symmetric point source. - We assume a homogeneous fluid with cylindrical co-ordinates r and z (see fig. 2.1). This choice of co-ordinates will prove advantageous for studying a layered Earth in later considerations. We will, also, take this opportunity to develop some mathematical tools which will prove useful. The wave equation in cylindrical co-ordinates with no azi-

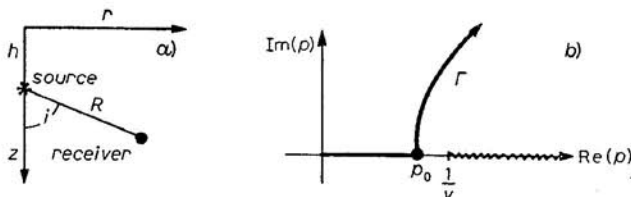


Fig. 2.1. — Source-receiver geometry (a)) and complex p -plane (b)) with branch cut starting at $1/V$ and running out along the real p -axis.

muthal dependence is

$$(2.1) \quad d^2\varphi/dr^2 + (1/r)d\varphi/dr + d^2\varphi/dz^2 - (1/\alpha^2)d^2\varphi/dt^2 = 0,$$

where φ is the displacement potential and α the compressional velocity. Taking the Laplace transform of (2.1) yields

$$(2.2) \quad d^2\tilde{\varphi}/dr^2 + (1/r)d\tilde{\varphi}/dr + d^2\tilde{\varphi}/dz^2 - (s^2/\alpha^2)\tilde{\varphi} = 0,$$

where s is the Laplace-transform variable. A solution of (2.2) which is easily demonstrated by substitution is

$$(2.3) \quad \tilde{\varphi}(r, z, s) = J_0(kr) \exp[\pm\nu z],$$

where k is the horizontal wave number $\nu = (k^2 + s^2/\alpha^2)^{1/2}$ and J_0 the zeroth-order Bessel function. A more general expression is

$$(2.4) \quad \tilde{\varphi}(r, z, s) = \tilde{f}(s) \int_0^\infty J_0(kr) [A(k) \exp[-\nu z]] dk,$$

where we take the positive square root of ν and consider the solution which converges for large z . The functions $A(k)$ and $\tilde{f}(s)$ are arbitrary with respect to the operations in (2.2).

In the vicinity of the source the displacement potential must satisfy the known behavior of a spherical wave which is

$$(2.5) \quad \varphi_s = \begin{cases} 0, & t < R/\alpha, \\ (1/R)f(t - R/\alpha), & t > R/\alpha. \end{cases}$$

Taking the Laplace transform of (2.5) yields

$$(2.6) \quad \tilde{\varphi}_s(R, s) = (1/R) \exp[-(s/\alpha)R] \tilde{f}(s).$$

The question now is how to find the wave solution (2.4). A trick originated

$$(2.7)$$

which is easily proved. This trick is sometimes used in solving the wave equation in cylindrical coordinates. It comes

$$(2.8)$$

Of course, the inverse transform. We will use the Hoop transform model. We make use of functions to model

$$(2.9)$$

The solution becomes

$$(2.10) \quad \tilde{\varphi}(r, z, s) = \tilde{f}(s) \int_0^\infty J_0(kr) [A(k) \exp[-\nu z]] dk,$$

where $\eta = (1/\alpha^2)^{1/2}$.

This expression is valid for the real p -axis ($s = \eta p$).

$$(2.11) \quad \tilde{\varphi}(r, z, s) = \tilde{f}(s) \int_0^\infty J_0(kr) [A(k) \exp[-\nu z]] dk,$$

Equation (2.11) is the solution to discuss. Using the properties of the Bessel functions we have

$$(2.12) \quad K_n(x) = \frac{1}{2} \int_0^\infty J_0(kx) e^{-nk} dk,$$

The question now is can we find a way to match this condition (2.6) with the wave solution (2.4) in terms of $\varphi(r, z, s)$. This can be accomplished by using a trick originated by LAMB [6]. The needed identity is

$$(2.7) \quad \frac{\exp[-(s/\alpha)R]}{R} = \int_0^\infty J_0(kr) \exp[-\nu|z-h|] \frac{k}{\nu} dk,$$

ith branch cut

which is easily proven with the aid of the Fourier-Bessel theorem. This equation is sometimes referred to as the Sommerfeld integral representation. Thus the solution in cylindrical co-ordinates for an arbitrary time history, $f(s)$, becomes

$$(2.8) \quad \bar{\varphi}(r, z, s) = \bar{f}(s) \int_0^\infty J_0(kr) \exp[-\nu|z-h|] \frac{k}{\nu} dk.$$

Of course, the inverse Laplace transform of (2.8) must yield the (2.5) description. We will produce this result by performing the so-called Cagniard-de Hoop transformation, a technique that proves useful in the layered Earth model. We make a change of variable $k = -isp$ which transforms Bessel functions to modified Bessel functions, namely

$$(2.9) \quad J_0(-isp) \rightarrow (i/\pi) K_0(spr) - (i/\pi) K_0(-spr).$$

The solution becomes, after STRICK [7],

$$(2.10) \quad \bar{\varphi}(r, z, s) = -i \frac{f(s)s}{\pi} \int_{-i\infty+\delta}^{+i\infty+\delta} K_0(spr) \exp[-s\eta|z-h|] \frac{p dp}{\eta},$$

where $\eta = (1/\alpha^2 - p^2)^{1/2}$.

This expression can be further simplified by noting the symmetry across the real p -axis (Schwarz principle of reflection) obtaining

$$(2.11) \quad \bar{\varphi}(r, z, s) = f(s) \frac{2}{\pi} (s) \operatorname{Im} \int_\delta^{i\infty+\delta} K_0(spr) \exp[-s\eta|z-h|] \frac{p dp}{\eta}.$$

Equation (2.11) can be solved exactly, but there are some useful approximations to discuss. Using the asymptotic expansion ((9.7.2) of Abramowitz and Stegun), we have

$$(2.12) \quad K_n(x) = \left(\frac{\pi}{2x}\right)^{1/2} \exp[-x] \left[1 + \frac{\mu-1}{8x} + \frac{(\mu-1)(\mu-9)}{2(8x)^2} + \dots\right],$$

$t < R/\alpha$,

$t > R/\alpha$.

sust satisfy the

solution which
with respect to

where $\mu = 4n^2$. Keeping the first term only, we obtain

$$(2.13) \quad \bar{\varphi}(r, z, s) = \sqrt{\frac{2}{\pi rs}} \frac{f(s)}{s} \operatorname{Im} \int_0^\infty \frac{\sqrt{p}}{\eta} \exp [-s(pr + \eta|z - h|)] dp.$$

For simplicity, suppose we assume that $f(s) = 1/s$ or that the original source time history is a step function. The delta-function response can be determined later by taking a time derivative and the response for any arbitrary source by convolution. The integral in (2.13) occurs so often in generalized ray theory that it is worthwhile to discuss a rather ingenious trick for obtaining its solution (see [8]). From line source theory, we have

$$(2.14) \quad \tilde{\psi}(r, z, s) = \operatorname{Im} \int_0^\infty \exp [-s(pr + \eta|z - h|)] \frac{dp}{\eta}.$$

Note that this integral looks much like the formal definition of the Laplace transform, namely

$$\bar{g}(s) = \int_0^\infty \exp [-st] g(t) dt.$$

This identification leads one to the following change of variable:

$$(2.15) \quad t = pr + (1/\alpha^2 - p^2)^{1/2}|z - h|.$$

Solving for $p(t)$ by applying the quadratic formula, we obtain

$$(2.16) \quad \begin{cases} p = (r/R^2)t - (R^2/\alpha^2 - t^2)^{1/2}|z - h|/R^2, & t < R/\alpha, \\ \eta = |z - h|/R^2t + (R^2/\alpha^2 - t^2)^{1/2}r/R^2, & \end{cases}$$

and

$$(2.17) \quad \begin{cases} p = (r/R^2)t + i(t^2 - R^2/\alpha^2)^{1/2}|z - h|/R^2, & t > R/\alpha. \\ \eta = |z - h|t/R^2 - i(t^2 - R^2/\alpha^2)^{1/2}r/R^2, & \end{cases}$$

Taking the derivative of (2.16), we obtain

$$(2.18) \quad \frac{dp}{dt} = \frac{r}{R^2} + i \left(t^2 - \frac{R^2}{\alpha^2} \right)^{-1} \frac{|z - h|t}{R^2} = \frac{i\eta}{(t^2 - R^2/\alpha^2)^{1/2}}$$

and, similarly, f

$$(2.19)$$

We now perform real. Such a pat the imaginary ax analytic continua at ∞ is zero and

$$(2.20) \quad \tilde{\psi}(r, z, s)$$

and

where $H(t)$ indica
Returning to

$$(2.21)$$

where

and we have use

The convolution

which can be ev
complexity of J:
mation [9] and

$$J(\tau) =$$

and, similarly, from (2.16)

$$(2.19) \quad \frac{dp}{dt} = \frac{r}{R^2} + \left(\frac{R^2}{\alpha^2} - t^2 \right)^{-\frac{1}{2}} \frac{|z-h|t}{R^2} = \frac{\eta}{(R^2/\alpha^2 - t^2)^{\frac{1}{2}}}.$$

We now perform the integration in the p -plane such that t will be positive and real. Such a path is given in fig. 2.1b). The contour C that runs, say, along the imaginary axis slightly to right of the origin, from 0 to $i\infty$, is deformed by analytic continuation to the above contour Γ . The contribution from the arc at ∞ is zero and there are no enclosed poles. Thus

$$(2.20) \quad \tilde{\psi}(r, z, s) = \operatorname{Im} \int_C \exp [-s(pr + \eta|z-h|)] \frac{dp}{\eta} = \int_0^\infty \exp [-st] \operatorname{Im} \left(\frac{1}{\eta} \frac{dp}{dt} \right) dt$$

and

$$\psi(r, z, t) = \operatorname{Im} \left(\frac{1}{\eta} \frac{dp}{dt} \right) = \frac{H(t - R/\alpha)}{(t^2 - R^2/\alpha^2)^{\frac{1}{2}}},$$

where $H(t)$ indicates the step function.

Returning to (2.13), with $f(s) = 1/s$, we obtain

$$(2.21) \quad \varphi(r, z, t) = \sqrt{2/r} \frac{1}{\pi} [1/\sqrt{t} * J(t)],$$

where

$$J(t) = \operatorname{Im} \left(\frac{\sqrt{p}}{\eta} \frac{dp}{dt} \right)$$

and we have used

$$\mathcal{L}(1/\sqrt{t}) = \sqrt{1/s}.$$

$$\mathcal{L}(t^{-\frac{1}{2}}) = \sqrt{\frac{1}{s}}$$

$$\mathcal{L}\left(\frac{1}{\sqrt{t}}\right) = \sqrt{\frac{1}{s}}$$

$t < R/\alpha$,

$t > R/\alpha$.

The convolution operation indicated in (2.21) can be written

$$\int_0^t (t-\tau)^{-\frac{1}{2}} J(\tau) d\tau,$$

which can be evaluated either analytically or numerically, depending on the complexity of $J(t)$. In this simple case, we can use the first-motion approximation [9] and obtain

$$J(\tau) = \sqrt{p} (\tau^2 - R^2/\alpha^2)^{-\frac{1}{2}} H(\tau - R/\alpha) = \sqrt{r/2} \frac{1}{R} (\tau - R/\alpha)^{-\frac{1}{2}}$$

and

$$\int_0^t (t-\tau)^{-\frac{1}{2}} (\tau - R/\alpha)^{-\frac{1}{2}} d\tau = \pi H(t - R/\alpha).$$

Thus eq. (2.21) reduces to

$$\varphi(r, z, t) = \frac{1}{R} H(t - R/\alpha),$$

as it must (see [7] for more details). This operation is easily visualized by performing the convolution by graphical means (see fig. 2.2). Note that one simply multiplies the two functions together and sums from 0 to t . The answer

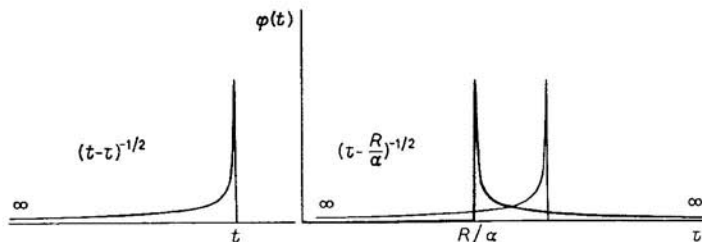


Fig. 2.2. — Schematic diagram explaining the convolution operation by graphical means. We reverse the direction of the square-root operation and perform the multiplication of the two functions for values of τ from 0 to t and sum. The results are zero until the two functions overlap.

remains zero until t reaches $t = R/\alpha$, where the two square-root singularities overlap and generate a step.

The solutions for more complicated models can be easily obtained with this technique. For instance, suppose we generate the step response appropriate for the interface problem (see fig. 2.3). There will be two generalized rays in the upper half-space required to solve the boundary conditions (see, for instance, [10] or [11]). There will be a direct generalized ray which is identical to the response just discussed plus a generalized ray that describes the response returning from the interface. The latter response can be written

$$(2.22) \quad \varphi(r, z, t) = \sqrt{2/r} \frac{1}{\pi} [1/\sqrt{t} * J(t)],$$

where

$$t = pr + \eta_1(z + h), \quad \eta_i = \left(\frac{1}{\alpha_i^2} - p^2 \right)^{\frac{1}{2}},$$

$$J(t) = \text{Im} \left(\frac{\sqrt{p}}{\eta_1} R(p) \frac{dp}{dt} \right),$$

$$R(p) = (\rho_2 \eta_1 - \rho_1 \eta_2) / (\rho_2 \eta_1 + \rho_1 \eta_2)$$

Fig. 2.3. — The r
Note that the gra
 $t = R/\alpha_1$ the squa
at $t = R/\alpha_1$, the

and dp/dt is the

where $R = ((z -$
a Snell's law re

If $\alpha_2 > \alpha_1$, t
will start before
becomes

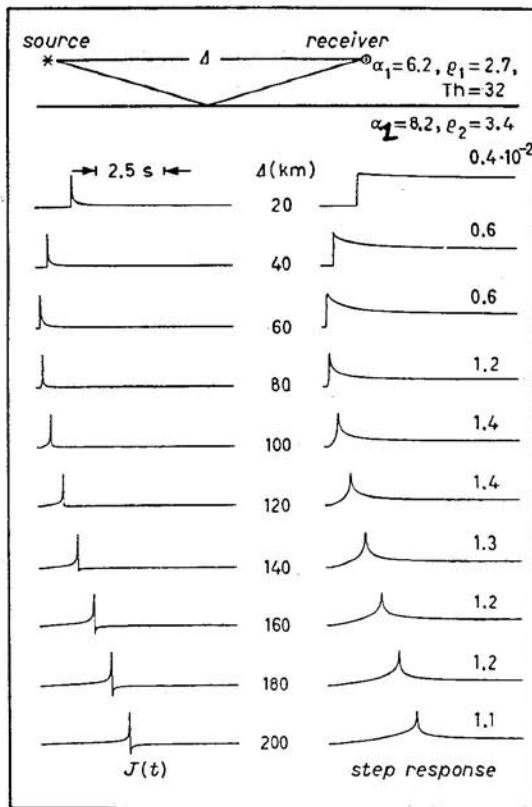


Fig. 2.3. — The responses of $J(t)$ and $\varphi(t)$ as a function of source-receiver separation. Note that the graphical convolution operator at the larger ranges has two parts; before $t = R/\alpha_1$ the square-root singularities are congruent and produce a logarithmic singularity at $t = R/\alpha_1$, the second part corresponds to a weighted step response as in fig. 2.2.

and $d\varphi/dt$ is the derivative along the I' contour, namely

$$\frac{d\varphi}{dt} = \begin{cases} \eta_1/(R^2/\alpha_1^2 - t^2)^{\frac{1}{2}}, & t < R/\alpha_1, \\ i\eta_1/(t^2 - R^2/\alpha_1^2)^{\frac{1}{2}}, & t > R/\alpha_1, \end{cases}$$

where $R = ((z + h)^2 + r^2)^{\frac{1}{2}}$, which corresponds to the distance traveled along a Snell's law reflected path.

If $\alpha_2 > \alpha_1$, there will be a critical angle and a head wave. In this case $J(t)$ will start before $t = R/\alpha$, since η_2 becomes complex at $p = 1/\alpha_2$ and $t_c(p = 1/\alpha_2)$ becomes

$$t_c = \frac{r}{\alpha^2} + \left(\frac{1}{\alpha_1^2} - \frac{1}{\alpha_2^2} \right)^{\frac{1}{2}} (z + h).$$

Evaluating (2.22) numerically, we obtain the step responses displayed in fig. 2.3. Physically, this technique computes the response by summing over all possible ray parameters p that interact with the boundary.

2.2. Shear dislocation (double-couple) source. — In this subsection we will examine some relatively simple dislocation models. Starting with Haskell's representation for shear faulting it is relatively easy to devise the displacements for double couples in an infinite medium (see [12]). The solution for a strike-slip fault becomes

$$(2.23) \quad \begin{cases} \bar{W}(r, z, \omega) = K \left[\frac{\partial}{\partial z} \left(\frac{\partial^2 A}{\partial r^2} - \frac{1}{r} \frac{\partial A}{\partial r} \right) \right] \sin 2\theta, \\ \bar{V}(r, z, \omega) = K \left[\frac{2}{r} \left(\frac{\partial^2 A}{\partial r^2} - \frac{1}{r} \frac{\partial A}{\partial r} \right) + k_p^2 \frac{\partial B}{\partial r} \right] \cos 2\theta, \\ \bar{Q}(r, z, \omega) = K \left[\frac{\partial}{\partial r} \left(\frac{\partial^2 A}{\partial r^2} - \frac{1}{r} \frac{\partial A}{\partial r} \right) + k_p^2 \frac{\partial B}{\partial r} \right] \sin 2\theta, \end{cases}$$

(2.25)

where W , V and Q are the displacements in the vertical, azimuthal and radial co-ordinates. The parameters are

$$A = \frac{\exp[-(s/\beta)R]}{R} - \frac{\exp[-(s/\alpha)R]}{R}, \quad B = \frac{\exp[-(s/\beta)R]}{R},$$

where R = distance between the source and the receiver, α, β = compressional and shear velocities and K = source strength. The spatial derivatives are introduced because of the double-couple nature of the source, and the A and B are simple point source representations as before. Using the Sommerfeld integral (2.7) and performing the appropriate algebra (see [13]), we can express the displacements along the vertical, tangential and radial co-ordinates as

$$(2.24) \quad \begin{cases} \hat{W} = \frac{\partial \hat{\phi}}{\partial z} + sp \hat{\Omega}, \\ \hat{V} = \frac{1}{r} \frac{\partial \hat{\phi}}{\partial \theta} - \frac{1}{sp r} \frac{\partial^2 \hat{\Omega}}{\partial z \partial \theta} - \frac{\partial \hat{\chi}}{\partial r}, \\ \hat{Q} = \frac{\partial \hat{\phi}}{\partial r} - \frac{1}{sp} \frac{\partial^2 \hat{\Omega}}{\partial r \partial z} + \frac{1}{r} \frac{\partial \hat{\chi}}{\partial \theta}, \end{cases}$$

where

where z , r and θ are the vertical, radial, polar angle co-ordinates, respectively. The P -wave potential φ , the SV -wave potential Ω and the SH -wave potential χ are expressed by:

ed in fig. 2.3.
r all possible

tion we will
ith Haskell's
placements
for a strike-

hal and radial

$\beta)R]$,

compressional
erivatives are
d the A and B
e Sommerfeld
), we can ex-
co-ordinates as

$$\left\{
 \begin{array}{l}
 \text{P-wave:} \\
 \hat{\phi} = + \frac{M_0}{4\pi\varrho} \frac{2}{\pi} \operatorname{Im} \int_{c-i\infty}^{c+i\infty} C_1(p) \frac{p}{\eta_\alpha} \exp[-s\eta_\alpha|z-h|] K_2(spr) dp \cdot A_1(\theta, \lambda, \delta) + \\
 + \frac{M_0}{4\pi\varrho} \frac{2}{\pi} \operatorname{Im} \int_{c-i\infty}^{c+i\infty} C_2(p) \frac{P}{\eta_\alpha} \exp[-s\eta_\alpha|z-h|] K_1(spr) dp \cdot A_2(\theta, \lambda, \delta) + \\
 + \frac{M_0}{4\pi\varrho} \frac{2}{\pi} \operatorname{Im} \int_{c-i\infty}^{c+i\infty} C_3(p) \frac{p}{\eta_\alpha} \exp[-s\eta_\alpha|z-h|] K_0(spr) dp \cdot A_3(\theta, \lambda, \delta); \\
 \\
 \text{SV-waves:} \\
 \hat{\Omega} = + \frac{M_0}{4\pi\varrho} \frac{2}{\pi} \operatorname{Im} \int_{c-i\infty}^{c+i\infty} SV_1(p) \frac{p}{\eta_\beta} \exp[-s\eta_\beta|z-h|] K_2(spr) dp \cdot A_1(\theta, \lambda, \delta) + \\
 + \frac{M_0}{4\pi\varrho} \frac{2}{\pi} \operatorname{Im} \int_{c-i\infty}^{c+i\infty} SV_2(p) \frac{p}{\eta_\beta} \exp[-s\eta_\beta|z-h|] K_1(spr) dp \cdot A_2 + \\
 + \frac{M_0}{4\pi\varrho} \frac{2}{\pi} \operatorname{Im} \int_{c-i\infty}^{c+i\infty} SV_3(p) \frac{p}{\eta_\beta} \exp[-s\eta_\beta|z-h|] K_0(spr) dp \cdot A_3; \\
 \\
 \text{SH-waves:} \\
 \hat{\chi} = + \frac{M_0}{4\pi\varrho} \frac{2}{\pi} \operatorname{Im} \int_{c-i\infty}^{c+i\infty} SH_1(p) \frac{p}{\eta_\beta} \exp[-s\eta_\beta|z-h|] K_2(spr) dp \cdot A_4 + \\
 + \frac{M_0}{4\pi\varrho} \frac{2}{\pi} \operatorname{Im} \int_{c-i\infty}^{c+i\infty} SH_2(p) \frac{p}{\eta_\beta} \exp[-s\eta_\beta|z-h|] K_1(spr) dp \cdot A_5;
 \end{array}
 \right. \quad (2.25)$$

where

- s = Laplace-transform variable,
- p = ray parameter,
- η_v = $(1/v^2 - p^2)^{1/2}$,
- h = depth of source,
- α = compressional velocity,
- β = shear velocity,
- ϱ = density,
- M_0 = seismic moment,

s, respectively.
ave potential χ

with the orientation constants given by

$$(2.26) \quad \begin{cases} A_1(\theta, \lambda, \delta) = \sin 2\theta \cos \lambda \sin \delta + \frac{1}{2} \cos 2\theta \sin \lambda \sin 2\delta, \\ A_2(\theta, \lambda, \delta) = \cos \theta \cos \lambda \cos \delta - \sin \theta \sin \lambda \cos 2\delta, \\ A_3(\theta, \lambda, \delta) = \frac{1}{2} \sin \lambda \sin 2\delta, \\ A_4(\theta, \lambda, \delta) = \cos 2\theta \cos \lambda \sin \delta - \frac{1}{2} \sin 2\theta \sin \lambda \sin 2\delta, \\ A_5(\theta, \lambda, \delta) = -\sin \theta \cos \lambda \cos \delta - \cos \theta \sin \lambda \cos 2\delta, \end{cases}$$

where

$$\begin{aligned} \theta &= \text{strike from the end of the fault plane,} \\ \lambda &= \text{rake angle,} \\ \delta &= \text{dip angle.} \end{aligned}$$

The vertical radiation patterns, as will become apparent shortly, are defined by

$$(2.27) \quad \begin{cases} C_1 = -p^2, & SV_1 = -\frac{\varepsilon p \eta_\beta}{\beta^2} \sin \theta \cos \delta, \\ C_2 = 2\varepsilon p \eta_\alpha, & SV_2 = \frac{1}{\beta^2(1-2\varepsilon p^2)} \eta_\beta^2 - p^2, \\ C_3 = p^2 - 2\eta_\alpha^2, & SH_1 = \frac{1}{\beta^2}, \\ & SH_2 = \frac{\varepsilon \eta_\beta}{\beta^2 p}, \\ & SV_3 = 3\varepsilon p \eta_\beta, \end{cases}$$

where

$$\varepsilon = \begin{cases} +1, & z > h, \\ -1, & z < h. \end{cases}$$

The displacement field for any orientation of a double couple (see fig. 2.4) is the sum of displacement fields of three particular orientations of the double

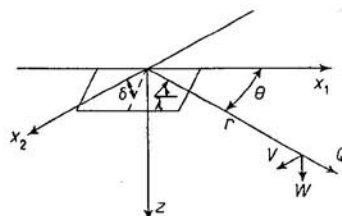


Fig. 2.4. - Co-ordinate system for the dislocation formulation where θ indicates the strike, δ the dip of the hanging wall and λ the motion of the hanging wall relative to the footwall.

couple, corresponds dip-slip fault (9)

The index and 3 45° dip

The integral domain by the For example, t

$$(2.28) \quad \zeta_n!$$

becomes

$$(2.29) \quad \zeta_n!$$

where

The geometric (see [8]). The choosing those where

The transformation subsection.

In this section since the equa HARKRIDER [1]

where the need to evalu grande later, of t after a ch of this type point spacing curaey of suc approximatio

couple, corresponding to the strike-slip fault ($\lambda = 0$ or 180° , $\delta = 90^\circ$), normal dip-slip fault ($90^\circ, 90^\circ$) and the dip-slip fault with a 45° dip ($45^\circ, 90^\circ$) (see [14]).

The index n in expression (2.27) corresponds to 1 strike-slip, 2 dip-slip and 3 45° dip-slip.

The integrals expressed in (2.25) can be transformed back into the time domain by the application of the Cagniard-de Hoop technique (see [15, 16]). For example, the field function defined by

$$(2.28) \quad \xi_n(r, z, s) = \frac{2}{\pi} s \operatorname{Im} \int_{c-i\infty}^{c+i\infty} \frac{p}{\eta_v} K_n(spr) \exp[-s\eta_v|z-h|] dp$$

becomes

$$(2.29) \quad \xi_n(r, z, t) = \frac{2}{\pi} \frac{\partial}{\partial t} \operatorname{Im} \int_0^t \frac{c_n(t, \tau)}{(t-\tau)^i(t-\tau+2pr)^i} \frac{dp}{d\tau} \frac{p(\tau)}{\eta_v} d\tau,$$

where

$$c_n(t, \tau(p)) = \cosh\left(n \cosh^{-1} \frac{t-\tau+pr}{pr}\right).$$

The geometry is given in fig. 2.1a) and the de Hoop contour in fig. 2.1b) (see [8]). The various functions of p are to be evaluated along Γ defined by choosing those values of p which make p real and monotonically increasing where

$$\tau(p) = pr + \eta_v|z-h|.$$

The transformation of p to τ follows from the algebra discussed in the last subsection.

In this simple case we have a closed-form solution for various values of η , since the equivalent form back in the (ω, k) domain has been evaluated by HARKRIDER [12]. For example,

$$\xi_2(r, z, t) = \frac{\partial}{\partial t} \left[\left(\frac{1}{R} + \frac{2V}{r^2} \left(t - \frac{R}{V} \right) \right) H\left(t - \frac{R}{V}\right) \right],$$

where the near-field contribution appears in terms of r . However, since we need to evaluate integrals similar to (2.25) with complicated complex integrands later, it should be noted that (2.29) can be evaluated for various values of t after a change of variable, as discussed earlier. A relatively fast evaluation of this type of integral is by nonuniform quadrature techniques where the point spacing is determined by the rate of change of the integrand. The accuracy of such techniques is discussed in [17]. We will examine some useful approximations by expanding the integrand of (2.29) in terms of $(t-\tau)^{-1}$.

$z > h$,
 $z < h$.
 (see fig. 2.4)
 of the double

η indicates the
 wall relative to

Note that

$$c_n(t, \tau, p) = \frac{1}{2} \frac{(y + (y^2 - 1)^{\frac{1}{2}})^{2n} + 1}{(y + (y^2 - 1)^{\frac{1}{2}})^n},$$

where

$$y = (t - \tau + pr)/pr,$$

and

$$\frac{c_n(t, \tau, p)}{(t - \tau + 2pr)^{\frac{1}{2}}} \approx \frac{1}{\sqrt{2pr}}$$

to first order. Thus we can approximate (2.29) by

$$(2.30) \quad \zeta_n(v, z, t) = \frac{2}{\pi} \frac{\partial}{\partial t} \operatorname{Im} \int_0^t \frac{1}{\sqrt{2pr}} \frac{1}{(t - \tau)^{\frac{1}{2}}} \frac{dp}{dt} \frac{p}{\eta_v} d\tau = \frac{d}{dt} \left[\frac{1}{\sqrt{t}} * \operatorname{Im} \left(\sqrt{2/r} \frac{1}{\pi} \frac{\sqrt{p}}{\eta_v} \frac{dp}{dt} \right) \right]. \quad (2.32)$$

This expression was obtained earlier by using the first term of the asymptotic form of the modified Bessel function. With this degree of accuracy, called the high-frequency solution, expressions (2.25) can be greatly simplified. We obtain

$$(2.31) \quad \begin{cases} \hat{\phi} = \frac{M_0}{4\pi\varrho} \sum_{j=1}^3 A_j(\theta, \lambda, \delta) \frac{2}{\pi} \operatorname{Im} \int_0^{+\infty} C_j \frac{p}{\eta_\alpha} \sqrt{\pi/2spr} \\ \cdot [\exp[-s(pr + \eta_\alpha|z - h|)] dp], \\ \hat{\Omega} = \frac{M_0}{4\pi\varrho} \sum_{j=1}^3 A_j(\theta, \lambda, \delta) \frac{2}{\pi} \operatorname{Im} \int_0^{+\infty} SV_j \frac{p}{\eta_\beta} \sqrt{\pi/2spr} \\ \cdot [\exp[-s(pr + \eta_\beta|z - h|)] dp], \\ \hat{\chi} = \frac{M_0}{4\pi\varrho} \sum_{j=1}^3 A_{(j+3)}(\theta, \lambda, \delta) \frac{2}{\pi} \operatorname{Im} \int_0^{+\infty} SH_j \frac{p}{\eta_\beta} \sqrt{\pi/2spr} \\ \cdot [\exp[-s(pr + \eta_\beta|z - h|)] dp], \end{cases} \quad (2.33)$$

where we are essentially assuming that the source duration, T , is

$$T \ll 2pr.$$

We still further approximate (2.30) by assuming

$$dp/dt = \frac{i\eta_v}{(t - t_s)^{\frac{1}{2}}(2t_s)^{\frac{1}{2}}}, \quad (2.34)$$

where $t_s = R/V$

called the first seismic distance 100 or greater (see [18]).

Transformin

Thus the po
of the $C_j(p)$, δ
 A_j 's. We will

2.3. Respon
generalized ray
solution, we ca

where

$D(t) =$

$\dot{D}(t) =$

$\Pi(t) =$

$\Sigma =$

For the case o
space

(2.34)

where $t_R = R/V$ and $p = p_0$ and (2.30) reduces to

$$\zeta_n(r, z, t) = \delta(t - t_R)/R,$$

called the first-motion approximation. This approximation is valid at teleseismic distances where the ratio of travel time to duration is of the order of 100 or greater and has proven quite useful in modeling shallow earthquakes (see [18]).

Transforming expressions (2.31) into the time domain, we obtain

$$(2.32) \quad \begin{cases} \varphi = \frac{M_0}{4\pi Q} \sum_{j=1}^3 A_j(\theta, \lambda, \delta) C_j \frac{H(t - R/\alpha)}{R}, \\ Q = \frac{M_0}{4\pi Q} \sum_{j=1}^3 A_j(\theta, \lambda, \delta) SV_j \frac{H(t - R/\beta)}{R}, \\ \chi = \frac{M_0}{4\pi Q} \sum_{j=2}^5 A_{j+3}(\theta, \lambda, \delta) SH_j \frac{H(t - R/\beta)}{R}. \end{cases}$$

Thus the potentials contain the classical vertical radiation patterns in terms of the $C_j(p)$, $SV_j(p)$ and $SH_j(p)$ and the horizontal pattern in terms of the A_j 's. We will use these expressions in discussing the teleseismic results later.

2.3. Response of a layer/half-space: digression. — Using the concepts of generalized ray theory and retaining only the first term of the asymptotic solution, we can construct the SH solution on a free surface, namely

$$(2.33) \quad V(r, 0, \theta, t) = \frac{M_0}{4\pi Q_0} \frac{d}{dt} \left[\dot{D}(t) * \sum_{j=1}^2 A_{j+3}(\theta, \lambda, \delta) V_j(t) \right],$$

where

$$V_j(t) = \sqrt{2/r} \frac{1}{\pi} \left[\frac{1}{\sqrt{t}} * \sum_{i=1}^n \text{Im} \left(\frac{\sqrt{p}}{\eta \beta} SH_i(p) \Pi(p) p \frac{dp}{dt} \right)_i \right],$$

$D(t)$ = dislocation history,

$\dot{D}(t)$ = far-field time function,

$\Pi(t)$ = product of the transmission and reflection coefficients,

\sum = summation over contributing rays.

For the case of a pure strike-slip dislocation embedded in a homogeneous half-space

$$(2.34) \quad V_j = V_1 = (2 \sin i / \beta^3) H(t - t_R)/R,$$

where i is the angle of incidence (see fig. 2.1a)). Substituting (2.34) into (2.33), we obtain

$$(2.35) \quad V = (M_0/4\pi\rho_0)(2F_0 \sin i/\beta^3) \cos 2\theta D(t - t_R)/\gamma R,$$

where the amplitude is given in centimeters with $F_0 = 10^{-20}$ for unit conversion, and the various parameters expressed as M_0 (erg), ρ_0 (g/cm³), β (km/s), R (km) and

$$\gamma = \int_0^\infty D(t) dt = D(\infty).$$

A factor of 2 has been introduced in the solution (2.35) by the *SH* free-surface receiver coefficient. The far-field step function response for a pure strike-slip event, $V_1(t)$, is given in fig. 2.5, where the model is included as an

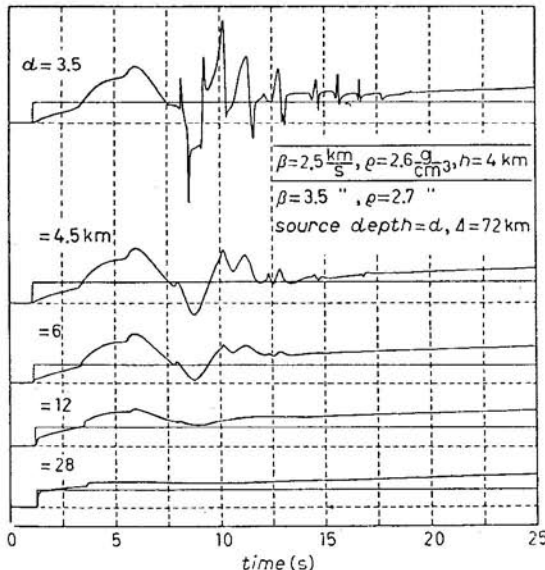


Fig. 2.5. – *SH* step function responses at the surface assuming a point strike-slip dislocation situated at various depths. The amplitudes are scaled relative to the top trace with the step response for a homogeneous half-space (bottom properties) displayed for comparison.

inset for various values of source depth. The corresponding half-space response is the simple step displayed on each trace. Comparing the response with the source situated just above ($d = 3.5$) and below ($d = 4.5$), one finds that the long-period behavior is nearly the same. The classical type of Love-wave dispersion is developed when the layer contains the source and is well understood in terms of ray interference. When the source is located below the layer, the

interpretation is rays. The ray c

with correspond

where the index space.

The coefficie

and

where

Each ray in determined by real and increasing t_1 , for the response plotted along $\text{Im}(dp/dt)$ lead

Note that 1 singularity yield tour is near v metric ray resp the saddle point up to ∞ . Thus An example a fig. 2.7. The occurring in t in this particu

into (2.33),

t conversion,
, $R(\text{km})$ and

the SH free-
for a pure
cluded as an

interpretation is more difficult, but can be studied by examining the various rays. The ray descriptions become

$$\begin{aligned}t_1 &= pr + \eta_2(d - h) + \eta_1 h, \\t_2 &= pr + \eta_2(d - h) + \eta_1(3h), \\t_n &= pr + \eta_2(d - h) + \eta_1(2n - 1)h,\end{aligned}$$

with corresponding Π coefficients

$$\begin{aligned}\Pi_1 &= T_{21}(p), \\ \Pi_2 &= T_{21}(p) R_{12}(p), \\ \Pi_n &= T_{21}(p) R_{12}^{n-1}(p),\end{aligned}$$

where the index 1 refers to the layer parameters and 2 to the bottom half-space.

The coefficients are

$$R_{12}(p) = (\mu_1 \eta_1 - \mu_2 \eta_2) / (\mu_1 \eta_1 + \mu_2 \eta_2)$$

and

$$T_{21}(p) = 2\mu_2 \eta_2 / (\mu_1 \eta_1 + \mu_2 \eta_2),$$

where

$$\mu_1 = \rho_1 \beta_1^2, \quad \mu_2 = \rho_2 \beta_2^2.$$

Each ray in the solution must be evaluated along its own contour which is determined by inverting these polynomial equations $p(t_n)$, where t is positive real and increasing from 0 to ∞ . The contour used to compute the direct rays, t_1 , for the responses in fig. 2.5 are shown in fig. 2.6. The parameter t is, also, plotted along these contours and it is easy to see that abrupt increases in $\text{Im}(dp/dt)$ lead to arrivals in fig. 2.5.

Note that $\text{Im}(dp/dt)$ always starts with the square-root singularity. This singularity yields the geometric ray arrival. For large source depths, the contour is near vertical and the synthetic wave form closely resembles the geometric ray response. The first-motion approximation is actually equivalent to the saddle point approximation which assumes that the contour goes straight up to ∞ . Thus the first-motion approximation is useful for teleseismic studies. An example application of this technique of earthquake modeling is given in fig. 2.7. The observed displacement is from a simple strike-slip earthquake occurring in the Imperial Valley, California. The only unknown parameters in this particular situation were the depth and slip history, $D(t)$. After a dil-

oint strike-slip
ive to the top
ties) displayed

pace response
onse with the
ands that the
ove-wave dis-
ll understood
he layer, the

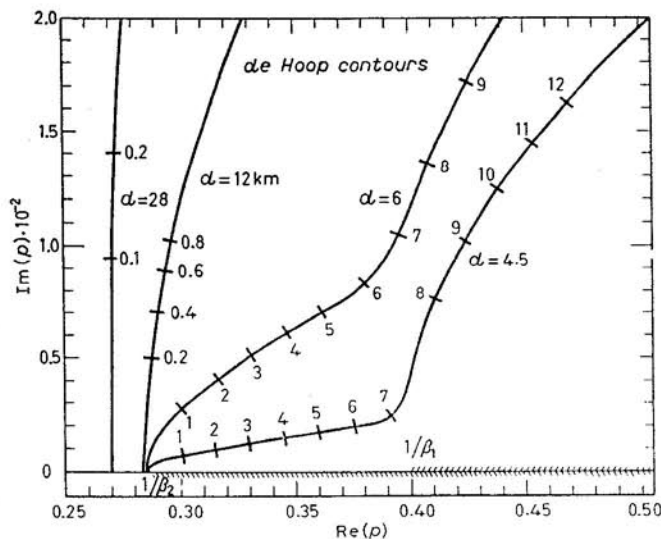


Fig. 2.6. - Contours of $\text{Im}(p)$ vs. $\text{Re}(p)$ for the direct rays shown in fig. 2.5. The branch cuts run along the $\text{Re}(p)$ co-ordinate, starting at $1/\beta_2$ and $1/\beta_1$, respectively. The parameter time is marked along each contour.

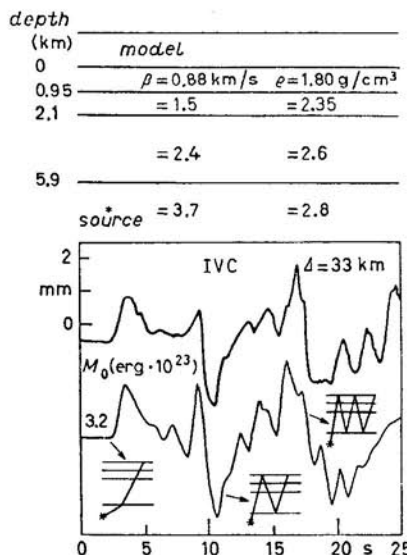


Fig. 2.7. - Comparison of a synthetic with a strong-motion recording, IVC, of an earthquake occurring at Brawley, Cal., in November 1976. The model parameters expressing the known structure are given at the top of the figure with the source at a depth of 6.9 km. The three most important rays are indicated schematically.

igent search, th
with duration
ducted by HEA
A rather com
tend to change
the first few b
predicted for f
or too large at t
in frequency co
variation in th
effects of a sin

Fig. 2.8. - Con
elastic paramet

particular case
produce high-f
3-dimensional

igent search, the source depth of 7 km and a $\dot{D}(t)$ specified by triangular pulse with duration 1.5 s was determined (see [19]). Similar studies have been conducted by HEATON and HELMBERGER [20] and HELMBERGER and MALONE [21]. A rather common observation in modeling multibounce phases is that they tend to change their character relatively rapidly. For instance, many times the first few bounces will appear nearly identical at neighboring stations, as predicted for flat layers. However, the next bounce will suddenly be missing or too large at these same stations. Another common feature is a sudden change in frequency content of the multiples. Such effects could be caused by lateral variation in the low-velocity waveguide near the surface. A simulation of the effects of a simple dipping interface is displayed in fig. 2.8 (see [22]). In this

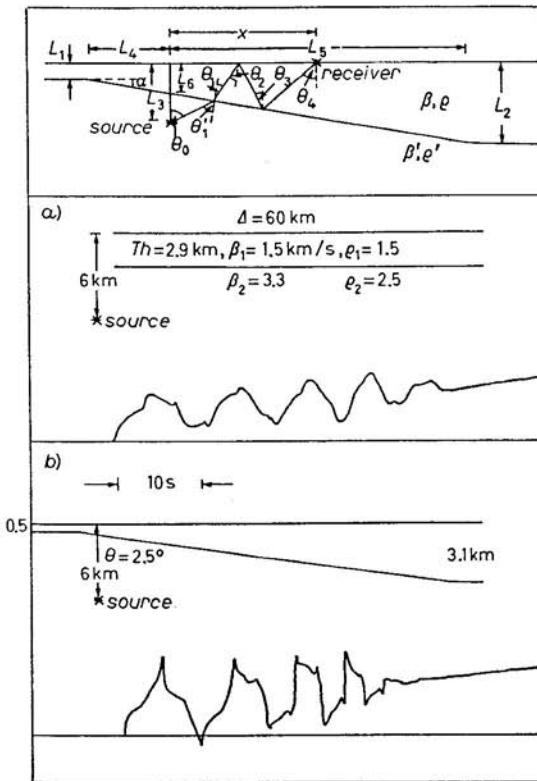


Fig. 2.8. – Comparison of the step responses for a flat and dipping layer where the elastic parameters are the same.

particular case, the rays can go beyond critical angle after bouncing and thus produce high-frequency reflections. Some progress on treating smoothly varying 3-dimensional structure is presented by HONG and HELMBERGER [22].

2.4. Full Cagniard solution. — The high-frequency solutions given by (2.31) have many advantages in model studies, as just discussed. However, for small values of spr , one must use the full solution by applying the transformation given in expression (2.29). The displacements are obtained by substituting expressions (2.25) into (2.24) and performing the Cagniard-de Hoop technique. The results are complicated because of the near-field terms. The tangential motions become

$$V(r, z, \theta, t) = \frac{M_0}{4\pi Q_0} \frac{d}{dt} \left[D(t) * \sum_{i=1}^2 A_{i+3} V_i \right],$$

$$V_1(r, z, \theta, t) = \frac{2}{\pi} \operatorname{Im} \int \int g_\beta(2) S H_1 R_T d\tau + \frac{2}{\pi} \operatorname{Im} \int \int g_\beta(2) S H_1 R_T \left(\frac{2}{pr} \right) d\tau dt + \\ + \frac{2}{\pi} \operatorname{Im} \int \int g_\alpha(2) C_1 R_{PT} \left(\frac{2}{r} \right) d\tau dt + \frac{2}{\pi} \operatorname{Im} \int \int g_\beta(2) S V_1 R_{TS} \left(\frac{2}{r} \right) d\tau dt,$$

where

$$R_T = p, \quad R_{PT} = 1, \quad R_{ST} = -\eta_\beta/p$$

for whole space and

$$R_T = 2p, \quad R_{PT} = \frac{4\eta_\alpha\eta_\beta}{\beta^2 R(p)}, \quad R_{ST} = \frac{-2\eta_\beta \eta_\beta^2 - p^2}{p \beta^2 R(p)}$$

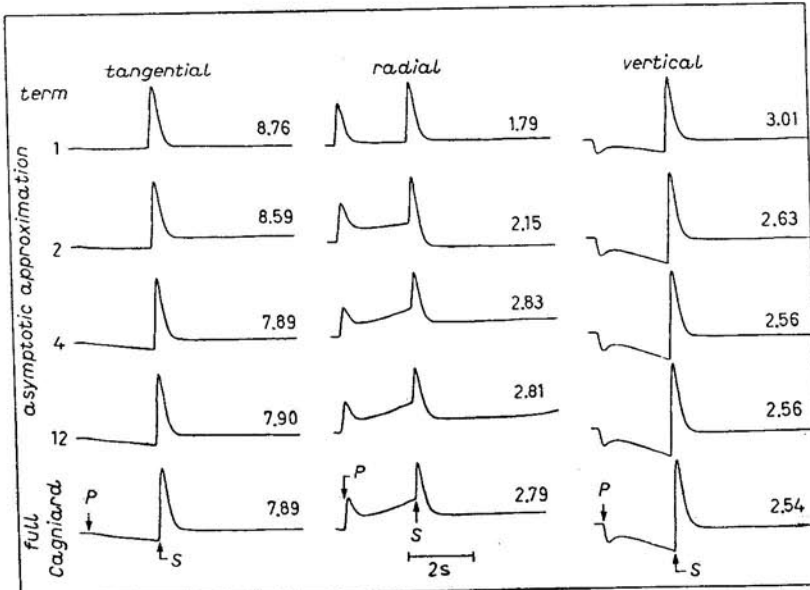


Fig. 2.9. — Comparison of the various components of motion for a strike-slip orientation at $\Delta = 16$ km for a whole space. The top four rows contain the asymptotic summation after 1, 2, 4 and 12 terms. The full solution is displayed on the bottom.

for a receiver
and where the

An evaluation
the near-field c
for comparison
data complicat
to the more us

3. — Modeling

Synthetic se
observations b
previous sectio
independent in
the free surface
elastic interact

Fig. 3.1. — Sch

fig. 3.1). Usin
appendix), we

$$(3.1) \quad W =$$

where

iven by (2.31)
ever, for small
transformation
y substituting
oop technique.
The tangential

THEORY AND APPLICATION OF SYNTHETIC SEISMOGRAMS

for a receiver on the free surface. The dip-slip result is similar with $n = 1$ and where the factor in parentheses is reduced by two.

An evaluation of this expression for a whole space is given in fig. 2.9, where the near-field contributions are apparent. The asymptotic solution is included for comparison. These computations are expensive and their applications to data complicated (see, for instance, [17, 23]). Thus we will limit our discussion to the more useful approximations where near-field terms can be neglected.

3. - Modeling at teleseismic distances.

Synthetic seismograms can be constructed for comparison with teleseismic observations by putting together the various suboperations discussed in the previous sections. We will be primarily interested in shallow events where independent information is many times available. Thus we must correct for the free surface. The simplest correction for this situation is to assume ideal elastic interaction and include the reflected phases, namely pP and sP (see

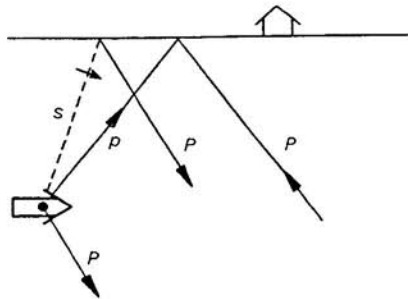


Fig. 3.1. - Schematic representation of the phases P , pP and sP .

fig. 3.1). Using expressions (2.24) and (2.32) and the concepts of GRT (see appendix), we can approximate the vertical response at the receiver

$$(3.1) \quad W = \frac{M_0}{4\pi\eta_0} \sum_{i=1}^3 \left[C_i(p_0) \delta(t) + C_i(p_0) R_{pp}(p_0) \delta(t - \Delta t_1) + S V_i(p_0) \frac{\eta_\alpha}{\eta_\beta} R_{sp}(p_0) \delta(t - \Delta t_2) \right] A_i \frac{R_{pz}(p_0)}{R},$$

where

$$\Delta t_1 = 2H\eta_\alpha, \text{ time lag of } pP,$$

$$\Delta t_2 = H(\eta_\alpha + \eta_\beta), \text{ time lag of } sP,$$

$$H = \text{source depth},$$

$$\dot{D}(t) = \delta(t), \text{ delta-function}.$$

strike-slip orienta-
e asymptotic sum-
n the bottom.

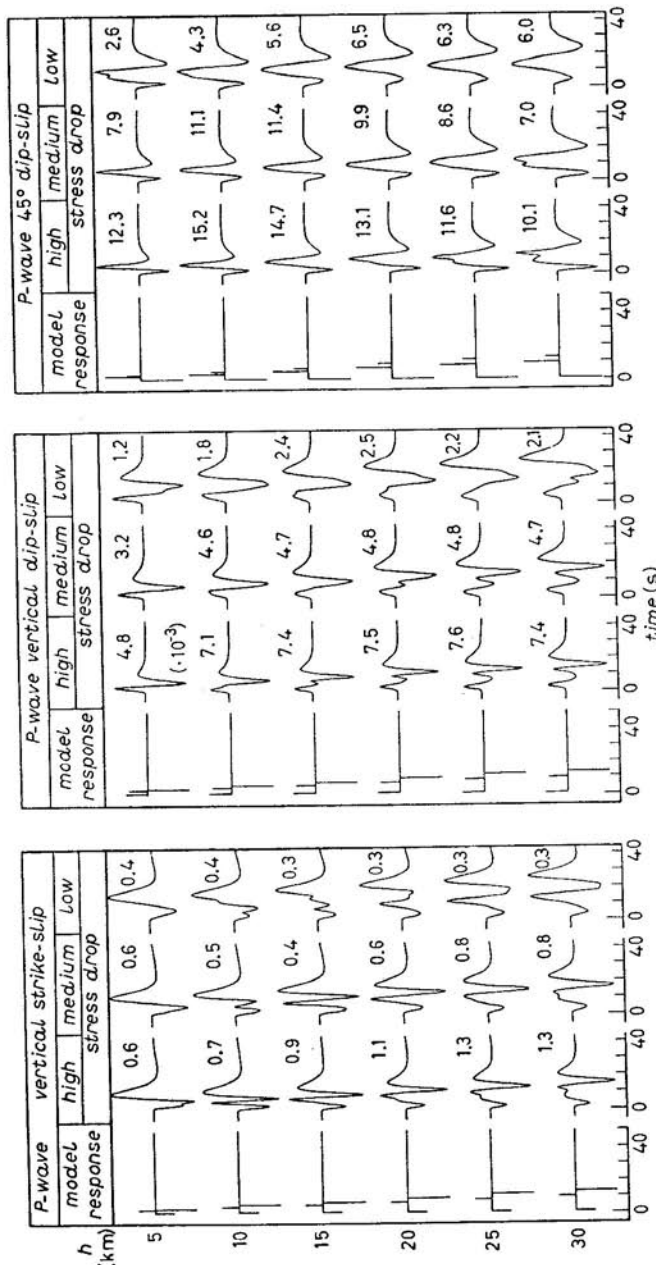


Fig. 3.2. — P -wave synthetic seismograms for the three potential terms with varying depth and time functions. The numbers to the upper right are actual potential amplitudes without the $M_0/4\pi g_0$, $1/R$ decay, and receiver functions included. The source time parameters, δt 's, are high stress-drop (0.5, 1.0, 0.5), medium stress-drop (1.0, 3.0, 1.0) and low stress-drop (2.0, 6.0, 2.0). After [18].

Fig. 3.3. — Graph

Fig. 3.4. — Obs Borrego Mount: represented by the Black dots indicated (downward determining the

Fig. 3.2. - P -wave synthetic seismograms for the three potential terms with varying $M_0/4\pi q_0$, $1/R$ decay, and receiver functions included. The source time parameters, δt 's, are high stress-drop (0.5, 1.0, 0.5), medium stress-drop (1.0, 3.0, 1.0) and low stress-drop (2.0, 6.0, 2.0). After [18].

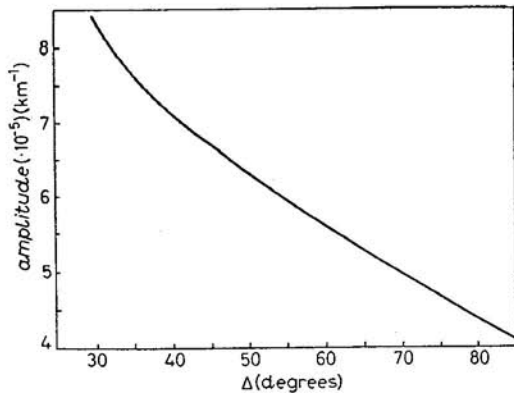


Fig. 3.3. - Graph of the effective $1/R$ decay in a Jeffreys-Bullen spherical Earth.

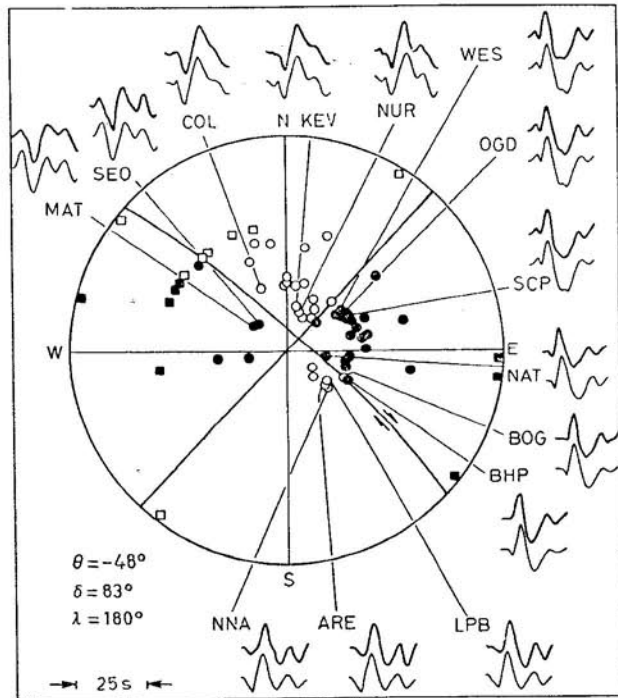


Fig. 3.4. - Observed (top) and synthetic (bottom) long-period P wave forms for the Borrego Mountain earthquake at 14 WWSS stations. The P first-motion plot is represented by the equal-area stereographic projection of the lower half of the focal sphere. Black dots indicate compression (upward breaking P) and open circles indicate dilatation (downward breaking P). The decay solid lines denote the nodal planes used in determining the fault orientation, θ (strike), δ (dip), λ (slip direction). Modified after [24].

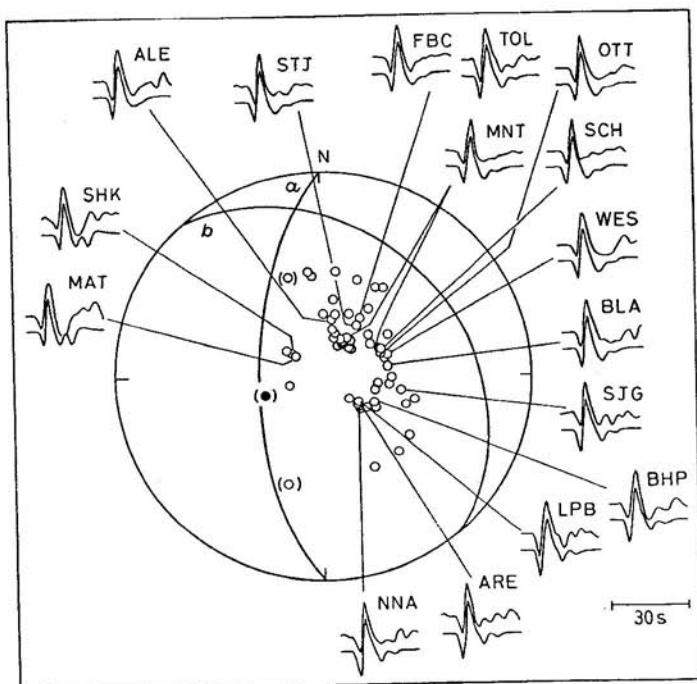


Fig. 3.5. – Focal-mechanism plot showing the P first motions for the Oroville earthquake, August 1, 1975. The observed P waveforms are given on the top and synthetic results on the bottom; \circ dilatation; nodal planes: a , $\theta = 180^\circ$, $\delta = 65^\circ$, $\lambda = -70^\circ$; b , $\theta = 319^\circ$, $\delta = 32^\circ$, $\lambda = -110^\circ$. Modified after [25].

The expression in brackets can be represented by three spikes with various strengths, depending on the source orientation, referred to as stick diagrams (see fig. 3.2). The diagram given in the first column displays this information, along with the timing of the three interacting phases P , pP and sP for the three fundamental faults. Crustal layering is easily incorporated by applying ray summations, as discussed in the previous section. We assume $t_a^* = 1$ and that the $1/R$ geometric spreading term in the homogeneous case can be replaced by the effective $1/R$ from fig. 3.3. The synthetics in fig. 3.2 were produced by performing the various convolutions assuming different source durations.

The wave shapes are seriously distorted by the interferences with each fault orientation having its own characteristics. Thus we can compare these synthetics with observed wave shapes such as those given in fig. 3.4-3.6 to determine the fault parameters, namely strike, dip, slip vector, fault depth, moment and δt 's (source time history). Note that for observations near nodes such as BOG and BHP (fig. 3.4) one finds difficulty in determining the polarity of the direct P , since it is nearly zero. In cases where $\delta \neq 90^\circ$ we expect sP to still contribute as at BOG since the dip-slip component is strong. Note the

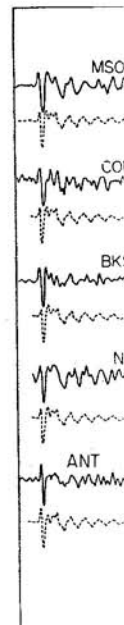


Fig. 3.6. – Foca quake, March 2- the vertical long initial simple ev-

strong difference position of the

Considerabl in oceanic env or situations w

Synthetics are nearly ide in wave shape samples of th distances. At complicated re prieate.

4. – Modeling

The region those beyond largely by the discontinuities

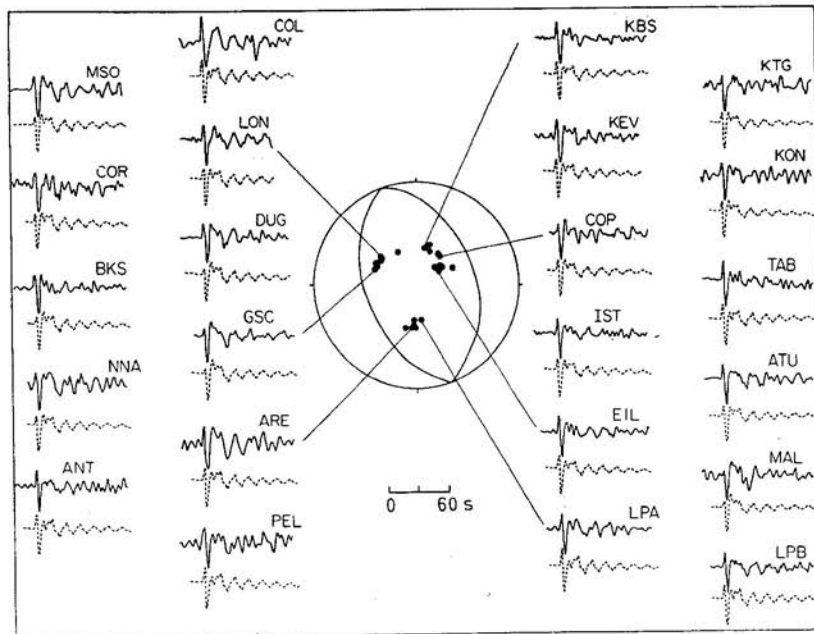


Fig. 3.6. — Focal mechanism plot showing the P first motions for the Bermuda earthquake, March 24, 1978. Observed (upper) and synthetic (lower) P -wave traces from the vertical long-period WWSSN seismograms for stations shown in fig. 1. Note an initial simple event followed by more complicated water reverberations. (After [26].)

strong differences in amplitudes displayed in fig. 3.2 which are caused by the position of the radiation loops.

Considerable ringing occurs for those events situated in some basins and in oceanic environments (see fig. 3.6 and [27] for examples of multipathing or situations where many rays are involved in generating the response).

Synthetics for normal and thrust faults are not very interesting, since they are nearly identical at all azimuths. As probably suspected, this uniformity in wave shape leads to a lack of resolution in fault orientation. We require samples of the energy release at other quadrants, in particular at regional distances. At these distances the Earth's mantle structure produces more complicated responses and the $(1/R)\delta(t - t_R)$ correction is no longer appropriate.

4. — Modeling regional body waves.

The regional phases can be subdivided into two groups, those less than and those beyond about 12° . At the smaller ranges the response is controlled largely by the crustal waveguide and at larger ranges by the upper-mantle discontinuities (see [28]).

4.1. Crustal waveguide. — We begin by discussing the effects of the crustal waveguide on the *P*-waves, actually all the energy that travels faster than the *S*-waves. This portion of the seismogram is commonly referred to as *P_n*, *PL* and *P_{nl}*. We assume a point shear dislocation, as before, and that the Earth can be treated by a single layer (crust) over a half-space (mantle) (see table I).

TABLE I. — *Crustal model.*

<i>P</i> velocity	<i>S</i> velocity	Density	Layer thickness
6.2	3.5	2.7	32.0
8.2	4.5	3.4	

Both of these assumptions are obvious oversimplifications but, as we will see, worth consideration as viable models at long periods. The vertical displacement, assuming the high-frequency solution, becomes

$$(4.1) \quad W(r, 0, \theta, t) = \frac{M_0}{4\pi\varrho_0} \frac{d}{dt} \left[\vec{D}(t) * \sum_{i=1}^3 A_i(\theta, \lambda, \delta) W_i(t) \right],$$

Fig. 4.2. — Rad-

going and sum-

where

(4.2) $W_i(t)$

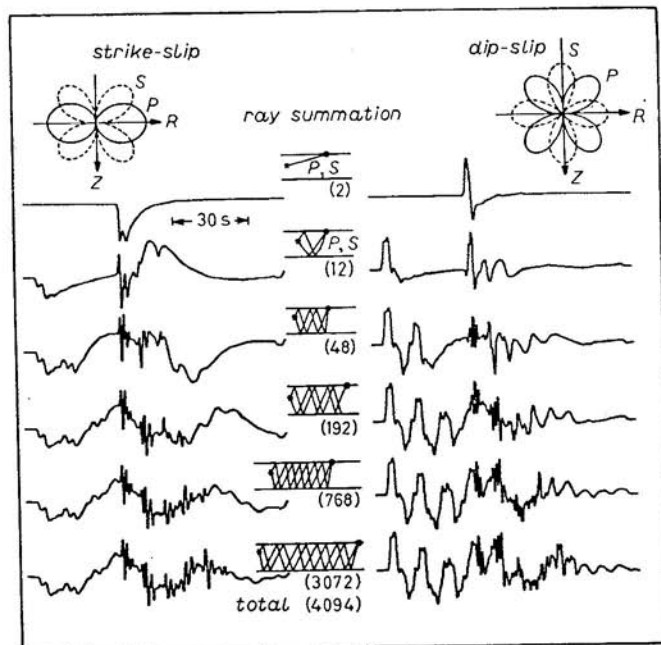


Fig. 4.1. — Vertical components of motion as a function of ray summation assuming a trapezoidal time function described by 0.5, 0.5, 0.5, for pure strike-slip and dip-slip orientations at $\Delta = 1000$ km.

where $R_{Nz}(p)$
or $S(N = S)$

radial
45° DS SS
vertical
45° DS SS
depth. The
meters assum

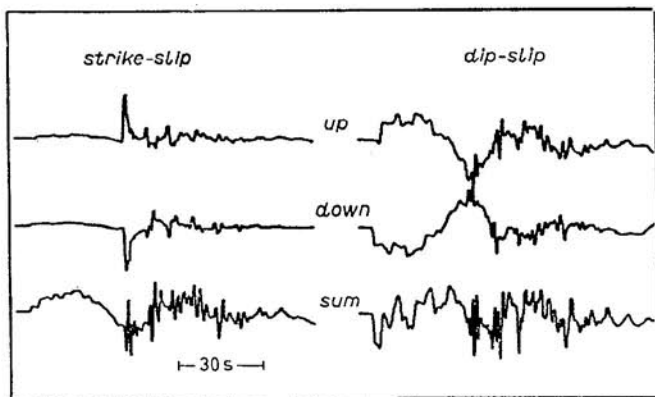
Fig. 4.3. — M

of the crustal faster than the to as P_n , PL that the Earth e) (see table I).

Layer thickness
32.0

as we will see, vertical displace-

Fig. 4.2. — Radial components of motion at $\Delta = 1000$ km in terms of upgoing, down-



going and summed for trapezoidal time history (0.5, 0.5, 0.5 s).

where

$$(4.2) \quad W_i(t) = \sqrt{2/r} \frac{1}{\pi} \left[\frac{1}{\sqrt{t}} * \sum_{i=1}^n \text{Im} \left(\frac{\sqrt{p}}{\eta_\alpha} C_i(p) R_{NZ}(p) \Pi_i(p) \frac{dp}{dt} \right) \right] + \\ + \sqrt{2/r} \frac{1}{\pi} \left[\frac{1}{\sqrt{t}} * \sum_{i=1}^n \text{Im} \left(\frac{\sqrt{p}}{\eta_\beta} SV_i(p) R_{NZ}(p) \Pi_i(p) \frac{dp}{dt} \right) \right],$$

where $R_{NZ}(p)$ indicates the appropriate receiver function for either P ($N = P$) or S ($N = S$) waves arriving at the station, respectively. The radial displace-

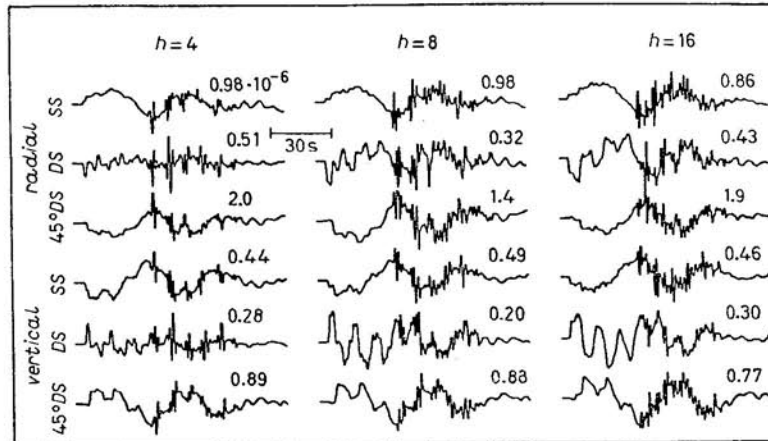


Fig. 4.3. — Motions of all three types of faults at $\Delta = 1000$ km as a function of source depth. The numbers above each trace indicate the zero-to-peak amplitude in centimeters assuming $M_0 = 4\pi Q_0 \cdot 10^{20}$ dyn·cm and trapezoidal time history (0.5, 0.5, 0.5 s).

mation assuming strike-slip and dip-slip

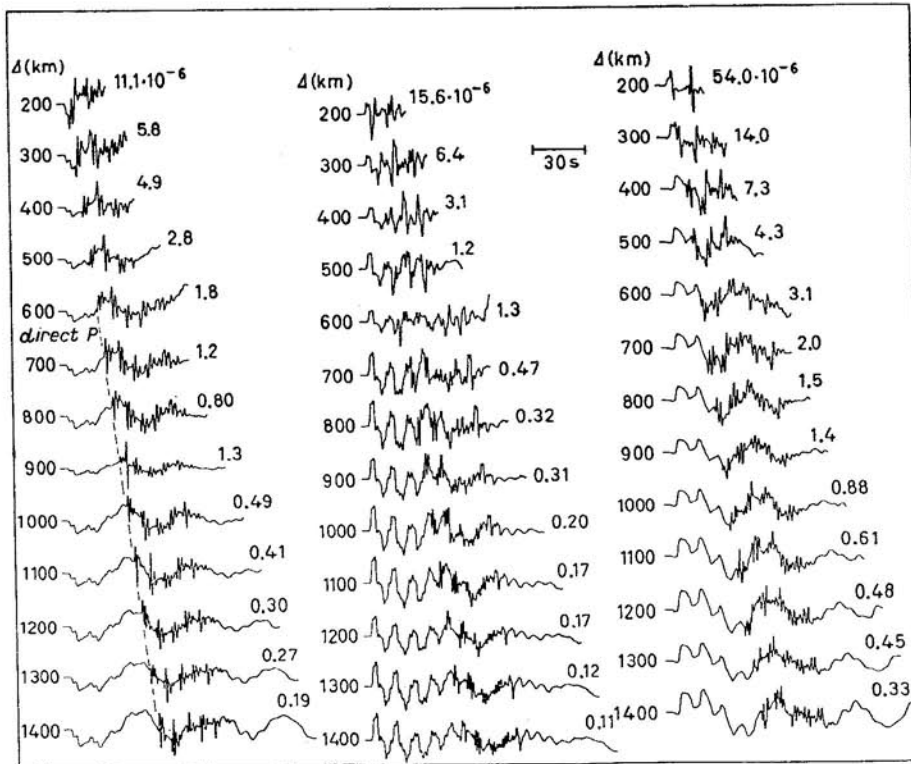


Fig. 4.4. -- Profiles of the vertical displacements for the three fundamental faults. The numbers above each trace indicate the zero-to-peak amplitude in centimeters assuming $M_0 = 4\pi Q_0 \cdot 10^{20}$ dyn·cm and trapezoidal time history (0.5, 0.5, 0.5 s). This time history was convolved with the delta-function response to reduce the high-frequency spikes created by the post-critical reflections so that the longer periods become more apparent. (After [31].)

ments, Q_i , are obtained by replacing R_{PZ} and R_{PR} with R_{SZ} and R_{SR} (see appendix for definitions of these receiver functions). The summation is over contributing rays where $\Pi_i(p)$ defines the product of all the reflection coefficients encountered along the ray path from the source to the receiver, similar to the SH case considered earlier. The strengths and polarities of the various rays are strongly influenced by the vertical radiation patterns, $C_i(p)$ and $SV_i(p)$; we have included these patterns above each column. Note that due to our limited time window we do not include the direct S pulse. The second pulse arriving in the direct ray response is actually a diffracted arrival, essentially the pulse that travels to the surface as a S -wave and along the surface as a P head wave. The first set of multibounce rays produces head waves along the top of the mantle. There are 12 rays in this set, namely

$$2^2 + 2^3 = 12,$$

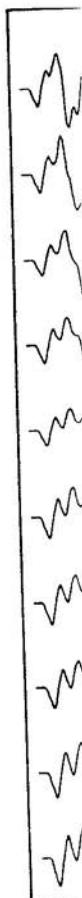
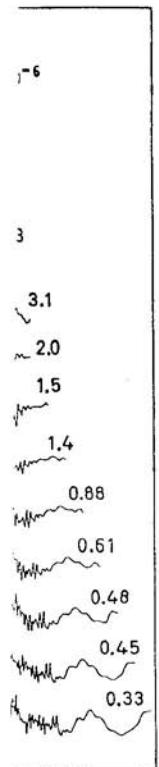


Fig. 4.5. -- The functions were convolved with a triangular fi

considering t
row were gen
ray set whic
For instance
bounce, sinc
amplitudes (

Another
contribution:
Changing th
trace produc
In fact, a go



lamental faults.
centimeters as
.5, 0.5 s). This
ce the high-fre-
periods become

d R_{SR} (see ap-
plication is over-
reflection coef-
-eiver, similar
of the various
 p) and $SV_s(p)$;
at due to our
e second pulse
val, essentially
e surface as a
aves along the

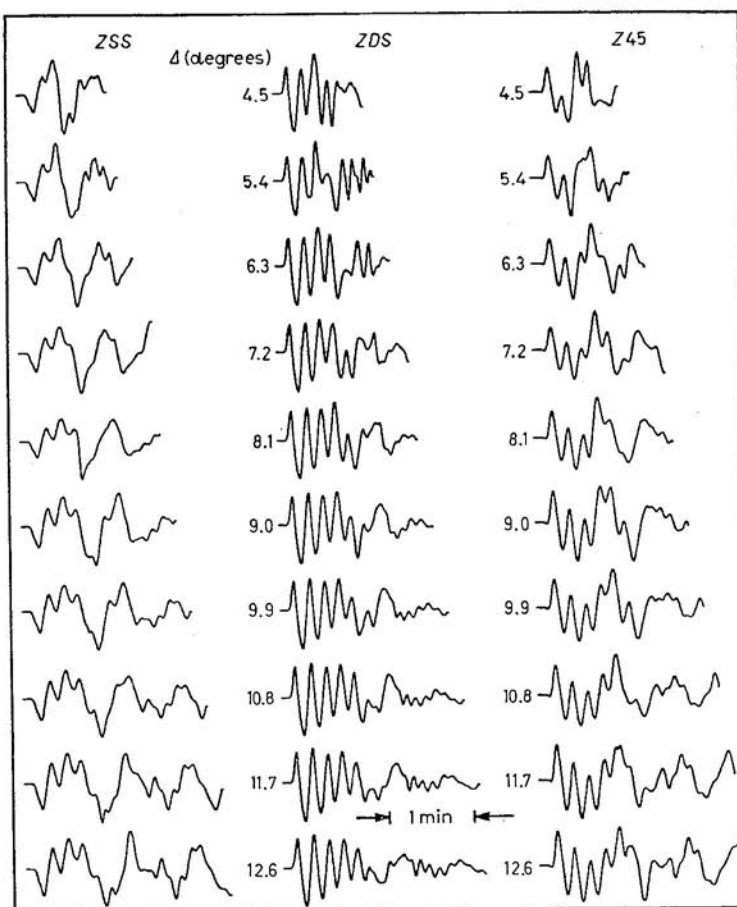


Fig. 4.5. – Theoretical displacement profiles for the vertical component. The Green's functions were computed from the model presented in table I and have been convolved with a source time function represented by a trapezoid ($t_1 = 1$, $t_2 = 1$, $t_3 = 1$), a triangular filter (2 s rise and fall) and a WWSSN long-period instrument.

considering the various possible mode changes. The responses in the bottom row were generated by summing all 4094 rays as a check against a much smaller ray set which takes advantage of the kinematic and dynamic redundancies. For instance, only 304 rays are needed to compute the response for the fifth bounce, since most of the rays in the complete set have the same times and amplitudes (see [29] or [11] for details).

Another strategy for understanding these motions is to split these ray contributions into those starting upward as opposed to downward (see fig. 4.2). Changing the source depth shifts the upgoing trace relative to the downgoing trace producing a dramatic effect on the dip-slip case, as displayed in fig. 4.3. In fact, a good approximate seismogram for $h = 4$ and 16 can be obtained by

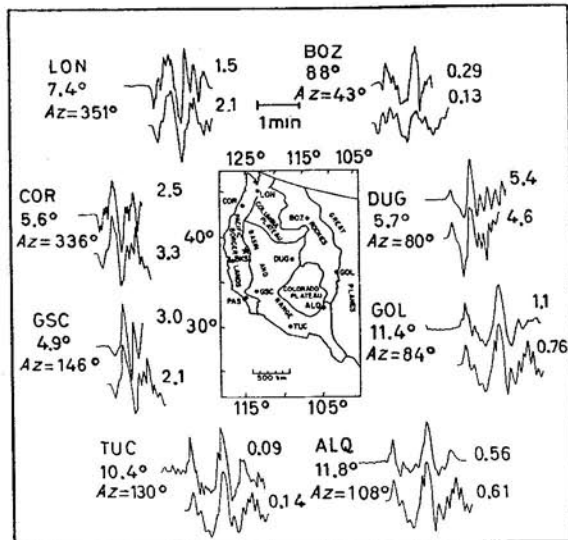


Fig. 4.6. – The vertical P_{nl} waveforms of the 1966 Truckee earthquake. The star denotes the epicenter. The data are the top trace at each station and the trace below is the synthetic fit. The strike-slip mechanism has two nodal planes which project through TUC and BOZ. To the right of each trace is the observed or predicted amplitude (on the basis of $M_0 = 0.8 \cdot 10^{25} \text{ dyn} \cdot \text{cm}$) in 10^{-3} cm .

simply shifting the $h = 8$ traces without recomputing the rays. Partial derivatives with respect to changes in velocities or changes in the waveguide can be approximated by stretching or compressing individual ray responses (see [30]).

For the purpose of studying source mechanisms we can apparently do reasonably well by assuming that common shallow earthquakes occur at a depth of 8 km. Profiles of responses for a dislocation located at this depth are presented in fig. 4.4. Preliminary comparisons of synthetics generated from these responses (see [31, 32]) indicate that these results are useful on a global scale if the high frequencies are removed. Thus we will filter these responses and the corresponding observations by convolving with a triangle which has a 2 s rise and fall. Convoluting these filtered Green's functions with a trapezoid source with 1 s intervals followed by the long-period WWSSN instrumental response yields the synthetics given in fig. 4.5. This time history is expected for events in the 5 to 6 magnitude class, the size commonly recorded by the network. We can, therefore, model shallow earthquakes at these ranges by simply forming a linear combination of these three fundamental synthetics. The relative strength of each column is used to fix the fault orientation, namely the strike, dip and slip vector. Some example comparisons of observations and corresponding synthetics are displayed in fig. 4.6-4.8. These results were found by applying a least-squares wave form inversion technique. The method

Fig. 4.7. – Filtered waveforms for the 1966 Truckee earthquake. The filter has a wavelength $\lambda = 275^\circ$. At each station the top trace is the observed waveform and the bottom trace is the synthetic fit.

involves an iterative process of fitting the synthetic to the observed waveform by the cross-correlation function. At each iteration, the relative strengths of the three primary moments are adjusted until the synthetic waveform closely matches the observed waveform. The results are discussed in section 4.6.

The Truckee earthquake produced excellent waveforms as typical for an event of magnitude $m_b = 5.7$ in this case. Tsunami waves, determined to have a wavelength of $\lambda = 275^\circ$, were recorded at stations and

V. HELMBERGER

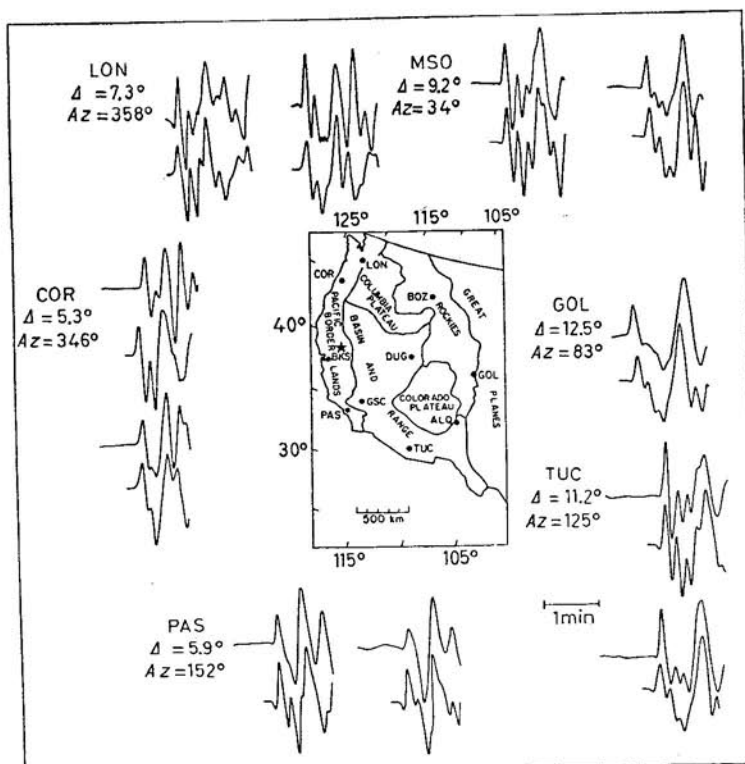


Fig. 4.7. - Filtered data and synthetics from the Oroville earthquake, $\theta = 204^\circ$, $\delta = 66^\circ$, $\lambda = 275^\circ$. At all the stations except GOL both the vertical (the first trace pair) and radial components are shown.

quake. The star
the trace below
s which project
predicted ampli-

s. Partial de-
the waveguide
ray responses

apparently do
es occur at a
at this depth
generated from
ful on a global
these responses
ngle which has
ith a trapezoid
instrumental
ry is expected
corded by the
ese ranges by
tal synthetics.
itation, namely
of observations
se results were
e. The method

involves an iterative scheme which makes use of an error function determined by the cross-correlation of the observed seismogram and a synthetic. Since only three parameters are involved, the scheme proves very effective. The moments are determined by simply comparing the amplitudes of the data with the synthetic and taking the average value. In general, the inversion yields results that are in good agreement with the literature. We will briefly discuss the Truckee event as an example.

The Truckee earthquake was a strike-slip event at 10 km depth which produced excellent regional records but very few teleseismic body wave records as typical of moderate-size strike-slip events. The Truckee earthquake ($m_b = 5.7$) has been studied by several authors [33, 34] making it a good test case. TSAY and AKI [33], from first-motion studies and modeling of the surface waves, determined this event to be pure strike-slip on a fault plane striking N 44° E and dipping 80° SE. The surface wave moment was determined to be $0.83 \cdot 10^{25}$ dyn·cm. Figure 4.6 shows the location of the epicenter, recording stations and filtered data for Truckee. Also shown are the synthetics deter-

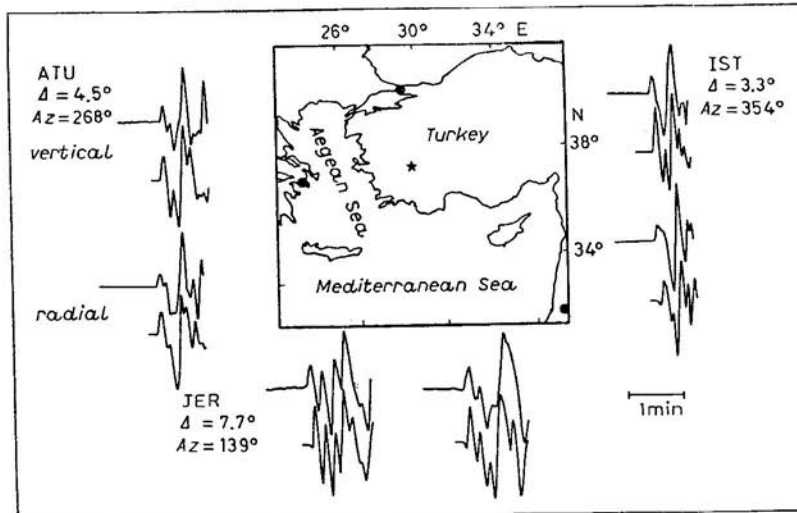


Fig. 4.8. – Location of the Turkey event (star) and the recording stations, $\theta = 131^\circ$, $\delta = 68^\circ$, $\lambda = 272^\circ$. The filtered data and synthetics for both the vertical and radial components are shown (after [30]).

mined from the inversion results. Note that BOZ and TUC are very nearly nodal. The inversion yields a mechanism which is very similar to Tsai and Aki's [33]; a strike of N 43° E, a dip of 76° SE and a rake of -11° . The only significant difference is the slight dip-slip component in our solution, which is also acceptable on the basis of the first-motion data. The moment determined from the P_{nl} wave forms is $0.87 \cdot 10^{25}$ dyn·cm, which is in agreement with [33].

The results for the Oroville earthquake are particularly interesting in that the observations are nearly all positive as opposed to those observed teleseismically (see fig. 3.5). We will discuss this event later after including the wave form observations in the 12° to 30° range.

4.2. Upper-mantle responses. – At distances larger than about 12° the mantle P -wave begins to emerge. This feature is displayed in fig. 4.9. Near 1000 km the beginning portion of the seismogram is dominated by P_n , that is a P head wave traveling along the top of the mantle as a head wave. Since this earthquake is nearly a pure strike-slip event, we can interpret the first upswing as P_n followed by pP_n and sP_n . Beyond about 12° this combination of arrivals becomes much sharper, since they are no longer head waves. Short-period waves from explosions fired at the Nevada Test Site increase in amplitude by nearly two orders of magnitude near this range (for example, see [35]). These features can be generally explained by the tectonic model presented in fig. 4.10. This smooth model is broken into homogeneous layers suitable for

Fig. 4.9. – Pro-
ALQ and LUB
others are of t

the applicati-
the interfaces
Synthetics a
recordings at
The pattern
apparent. C
thickness (tl
zone) may b
tween P_n an
 P_n in shield i
However, si
discussion to
quake obser
we omit rec
pendent to l
The resp

ST
= 3.3°
= 354°

tions, $\theta = 131^\circ$,
tical and radial

re very nearly
r to Tsai and
11°. The only
solution, which
moment deter-
s in agreement

resting in that
served teleseis-
ding the wave

about 12° the
fig. 4.9. Near
ed by P_n , that
ad wave. Since
erpret the first
is combination
d waves. Short-
increase in am-
ample, see [35]).
odel presented
ers suitable for

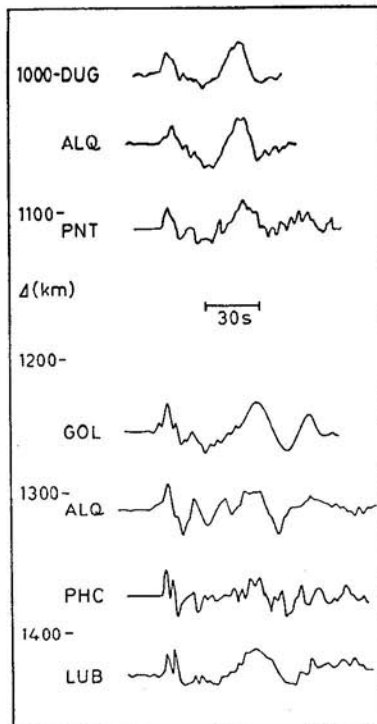


Fig. 4.9. — Profile of strike-slip observations from P_{nl} to P . Recordings at DUG, ALQ and LUB are from the 22 December 1964 event of northern Baja California, the others are of the Truckee event discussed earlier.

the applications of GRT. Essentially, the generalized rays returning from the interfaces in the mantle are added to the rays discussed earlier (see fig. 4.4). Synthetics appropriate for a strike-slip event are presented in fig. 4.11. The recordings at the nearest ranges are essentially the same as displayed in fig. 4.5. The pattern of P , pP and sP going from head waves to diving waves is quite apparent. Comparing these results with fig. 4.9 it would appear that the lid thickness (the high-velocity layers between the crust and the low-velocity zone) may be too thin in the T7 model. Actually, the crossover distance between P_n and P shows considerable lateral variation. For instance, short-period P_n in shield regions are observed to much larger distances than in other regions. However, since earthquakes rarely occur in shield regions, we will restrict our discussion to model T7 which appears to be quite useful in simulating earthquake observations in active regions (see, for example, [36]). Nevertheless, we omit records at ranges 12° to 14° as being too regional or structurally dependent to be useful in source modeling in most situations.

The response of the Earth models at ranges beyond 15° can be obtained

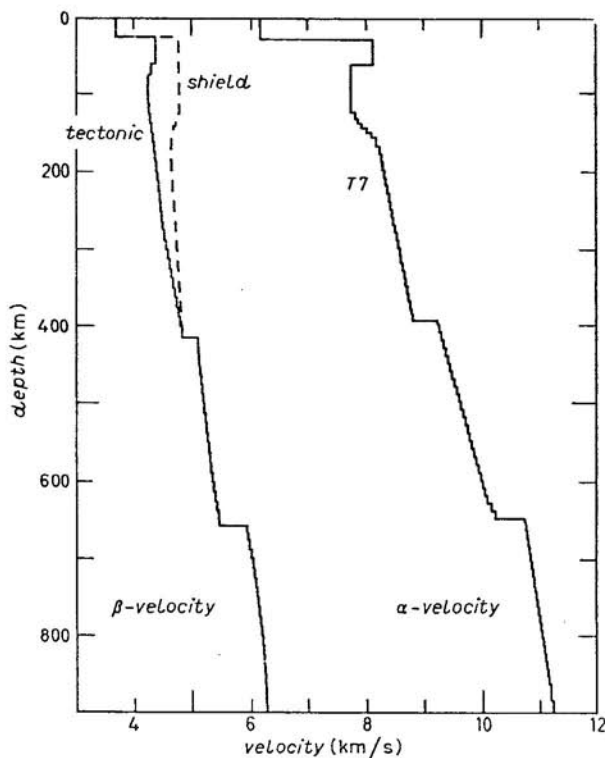


Fig. 4.10. — Velocity depth functions for T7 [37] and two recent shear wave models [38].

Fig. 4.11. — a) synthetics. b) synthetics.

metric formul

by simply summing primary rays. That is

$$(4.3) \quad M(t) = \sqrt{2/r} \frac{1}{\pi} \left(\frac{\Delta}{\sin \Delta} \right)^{\frac{1}{2}} \left[\frac{1}{\sqrt{t}} * J(t) \right],$$

(4.4)

where

$$J(t) = \sum_{i=2}^n \text{Im} \left(\frac{\sqrt{p}}{\eta_i} \left(\frac{dp}{dt} \right)_i \Pi_i(R, T) \right)$$

and

$$\Pi_2 = R_{12}, \quad \Pi_3 = T_{12}R_{23}T_{21}, \quad \text{etc.}$$

The term «primary» refers to rays that undergo one reflection only. The $\Delta/\sin \Delta$ factor is a correction for spherical spreading (see [15]).

Near 30° , $M(t)$ approximates a step with amplitude predicted by the curve in fig. 3.3. Actually, the amplitudes in fig. 3.3 were generated using expression (4.3) assuming the JB model. Similar results are obtained from the geo-

Because t
to document
done recently
reflectivity re
«full wave t»

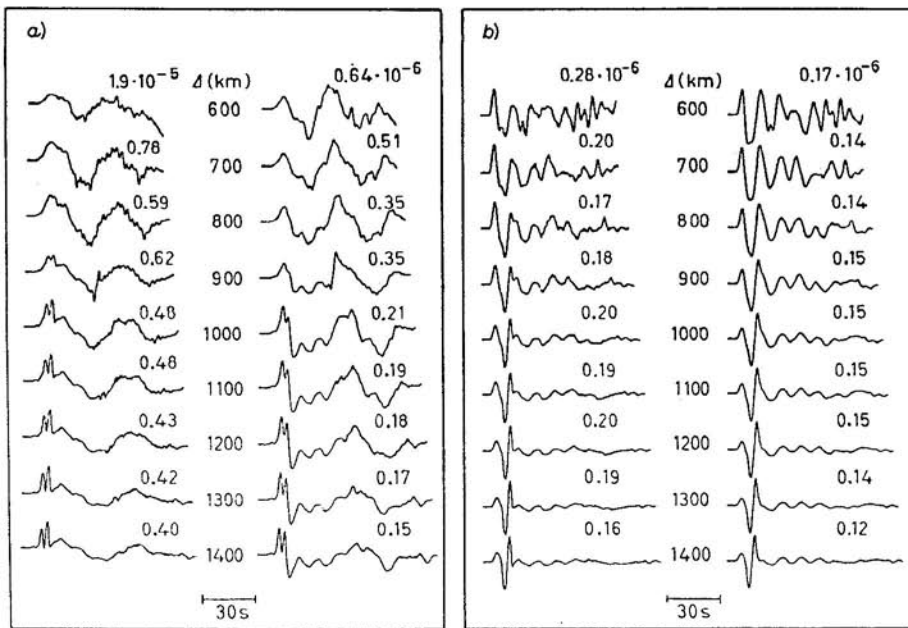


Fig. 4.11. -- a) Strike-slip excitation going from P_{ni} domination to P and long-period synthetics. b) Dip-slip excitation going from P_{ni} domination to P and long-period synthetics.

ent shear wave

metric formula ([39], p. 126)

$$(4.4) \quad A = \left[\frac{1}{r_0^2} \frac{v_0}{r_0} \frac{\operatorname{tg} i_0}{\cos i_0 \sin \Delta} \frac{1}{d\Delta^2} \frac{d^2 T}{d\Delta^2} \right]^{\frac{1}{2}},$$

where

- T is the travel time,
- Δ is the epicentral distance in degrees,
- i_0 is the angle of incidence,
- v_0 is the velocity at the surface,
- r_0 is the radius of the Earth.

Because the ray summation has omitted multiples, it appears necessary to document these responses by comparison with other methods. This was done recently by BURDICK and ORCUTT [40] with a comparison of GRT and reflectivity results given in fig. 4.12. These same responses were generated by «full wave theory» (see [41]) with similar wave forms.

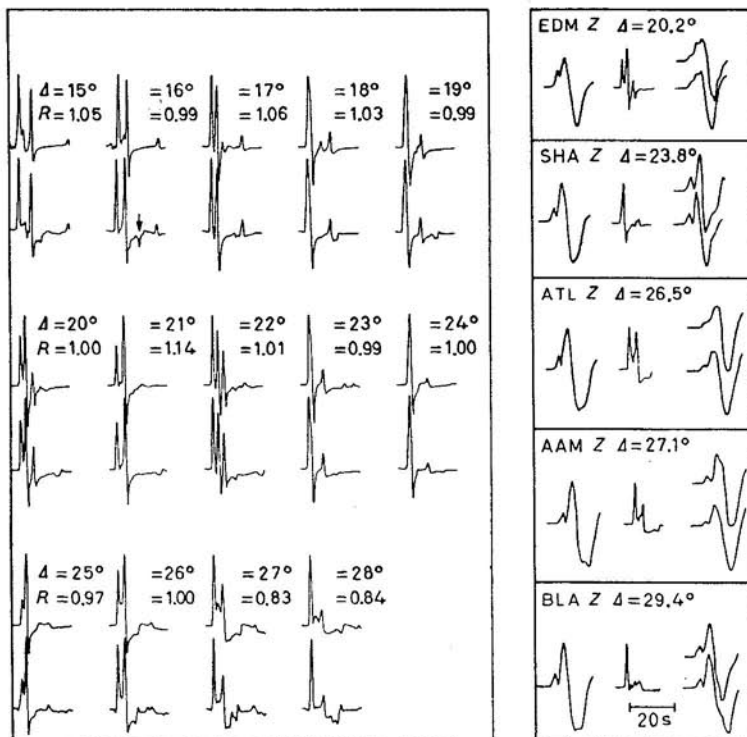


Fig. 4.12. — On the left, the slightly smoothed delta-function responses from a reflectivity calculation (bottom) are compared to those from a generalized ray (top) for model T7. On the right, the first column contains the predicted wave shape due to the source only; second column is the delta-function response of the model T7; third column is the convolution of the first two columns. The observed wave forms from the Borrego Mountain earthquake are on the top for comparison.

The vertical response for a dislocation source can be generated from $M(t)$ by assuming that the vertical radiation functions $C_j(p_0)$, etc. are nearly constant over the p 's involved, accordingly

$$(4.5) \quad W = \frac{M_0}{4\pi Q_0} \frac{d}{dt} \left[\dot{D} * \sum_{j=1}^3 A_j(\theta, \delta, \lambda) C_j(p_0) R_{PZ}(p_0) M(t) \right].$$

Similar approximations can be applied to generated pP , sP and crustal multiples. With this approximation, the procedure becomes identical to the teleseismic expression (3.1) where the factor $1/R$ is replaced with a convolution of $M(t)$ followed by a derivative. Synthetics appropriate for the three fundamental faults are displayed in fig. 4.13. A synthetic seismogram appropriate for any arbitrary orientation can then be formed by taking a linear combination of these three, as discussed earlier.

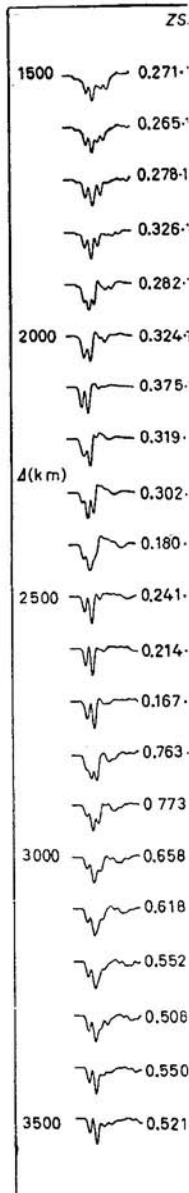


Fig. 4.13. — Fundamental orientation for the source

We can c
grams as if t
The first col



uses from a reflected ray (top) for the shape due to the LT7; third column comes from the Bor-

erated from $M(t)$ and is nearly constant

crustal multiples. In the teleseismic evolution of $M(t)$ three fundamental operations appropriate for any combination of

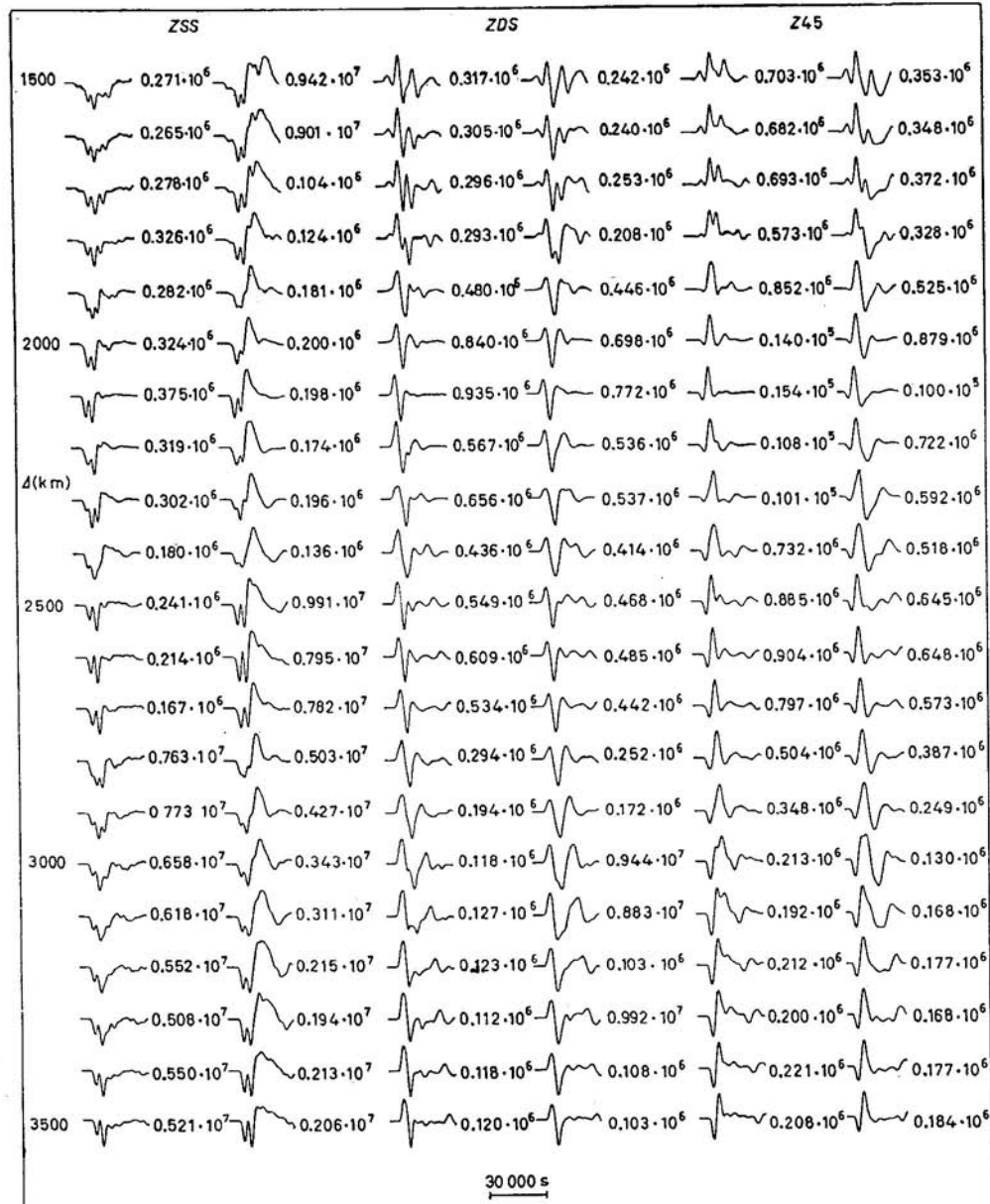


Fig. 4.13. — Upper-mantle synthetics without and with instrument for the three fundamental orientations assuming a source depth of 8 km, $t^* = 1$ and $\delta t_1 = \delta t_2 = \delta t_3 = 1$ for the source time history.

We can change the order of operations and generate the synthetic seismograms as if the $M(t)$ were a delta-function as under the teleseismic assumption. The first column of fig. 4.12b) corresponds to this order of operations. Con-

volving with the $M(t)$ produces the proper synthetic as given on the right of fig. 4.12b). The latter order of operations is generally used for studying upper-mantle structure, since $M(t)$ is isolated from the other operations.

5. — Discussion.

In this review, we have presented a procedure for generating synthetic wave forms for body phases. For convenience, we divided the epicentral distances into teleseismic, regional and local. At teleseismic distances, we showed

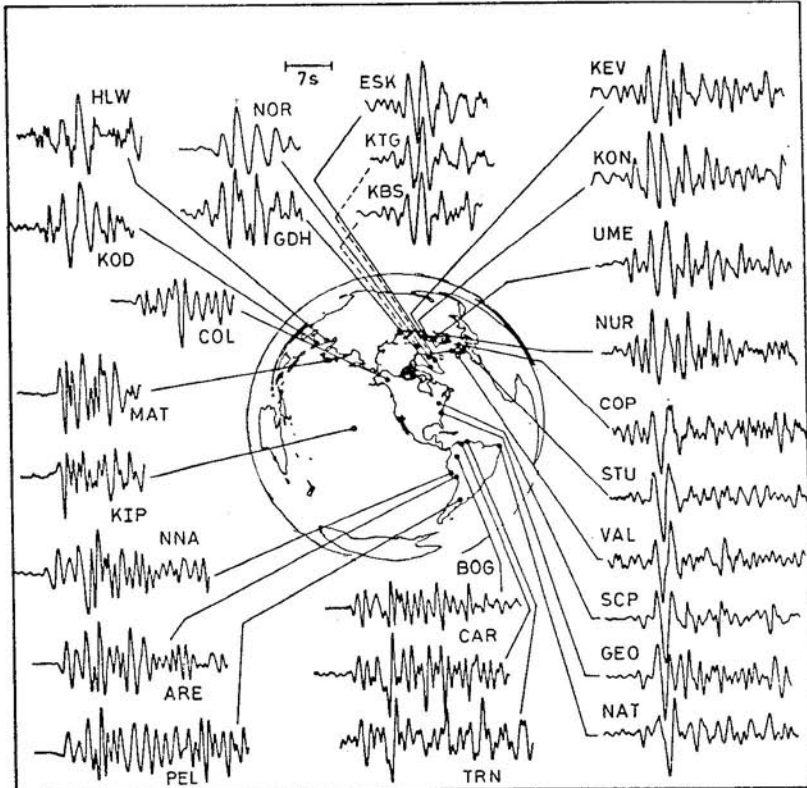


Fig. 5.1. — Short-period P wave forms for the Borrego Mountain earthquake recorded at WWSSN stations. Note the coherence of the first several seconds of the wave forms from stations at similar azimuths. The star denotes the location of the earthquake. (After [42].)

that long-period body phases from shallow earthquakes are coherent at neighboring stations and that the observed wave form could be decomposed in a

manner that many events in periods by assuming the signal was other hand, the neighboring stations (fig. 5.1). Some by EBEL and

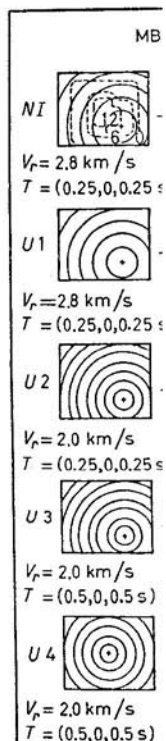


Fig. 5.2. — Comparison of observed seismic waveforms with calculated models for a particular dislocation and U_4 models

To model procedures to sample, [44, 45]

on the right of
studying upper-
ations.

ating synthetic
epicentral dis-
tances, we showed

manner that allows determination of faulting parameters. It appears that many events in the magnitude class 5.5 to 6.5 can be easily modeled at long periods by assuming point sources. This result should not be surprising, since the signal wavelengths are long compared to the fault dimensions. On the other hand, the corresponding comparison between short-period records at neighboring stations is much less coherent and complicated (see for example fig. 5.1). Some success at explaining these records has been presented recently by EBEL and HELMBERGER [42] by introducing complex faulting.

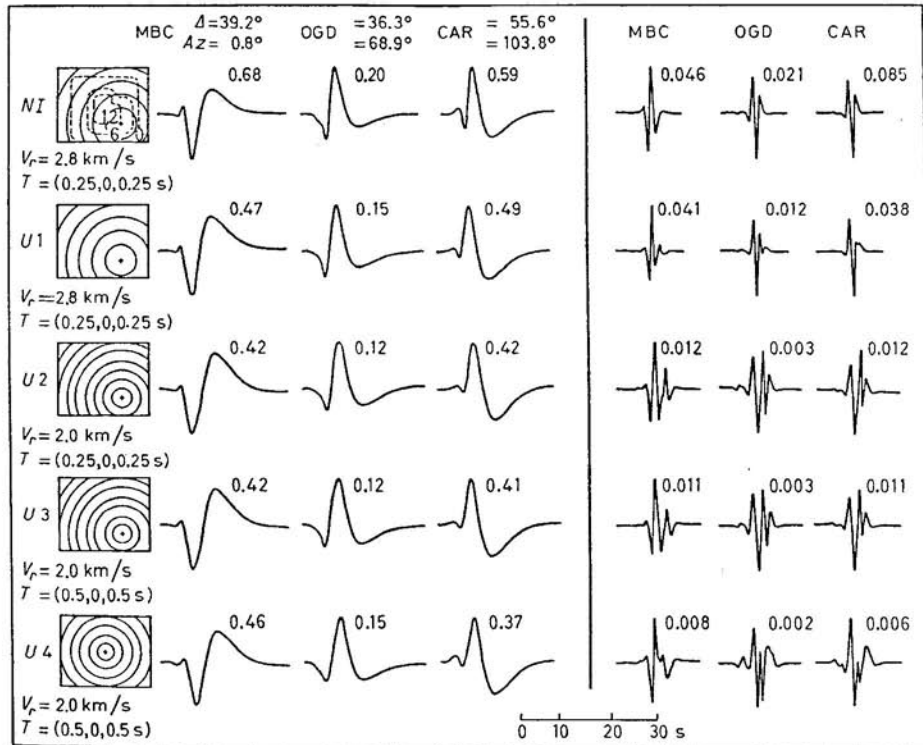


Fig. 5.2. – Comparison of the short-period and long-period synthetics at the teleseismic stations for various fault models. The numbers are the amplitudes in micrometres calculated for the seismic moment of $5 \cdot 10^{24} \text{ dyn} \cdot \text{cm}$. The top row corresponds to a particular distribution of faulting appropriate for the Coyote earthquake where the dislocation is largest at the center and tapers down at the edges. The U_1 , U_2 , U_3 and U_4 models show uniform slip histories but with different rupture speeds. (After [43].)

earthquake recorded
of the wave forms
of the earthquake.

coherent at neigh-
decomposed in a

To model shorter periods requires that we generalize our point source procedures to treat finite faults as distributed point sources (see, for example, [44, 45]). Following the latter technique we simply simulate rupturing

on a fault plane by summing point sources with the proper timing (see fig. 5.2). The procedure is made somewhat complicated by the presence of the free surface which requires summing pP , etc. Thus teleseismic signals can show considerable variation with azimuth. Note that the long-period records prove quite insensitive to the rupture properties in this simple case compared with

with respect particularly s frequency str in the time hi

At ranges come multiva features from can be seen i

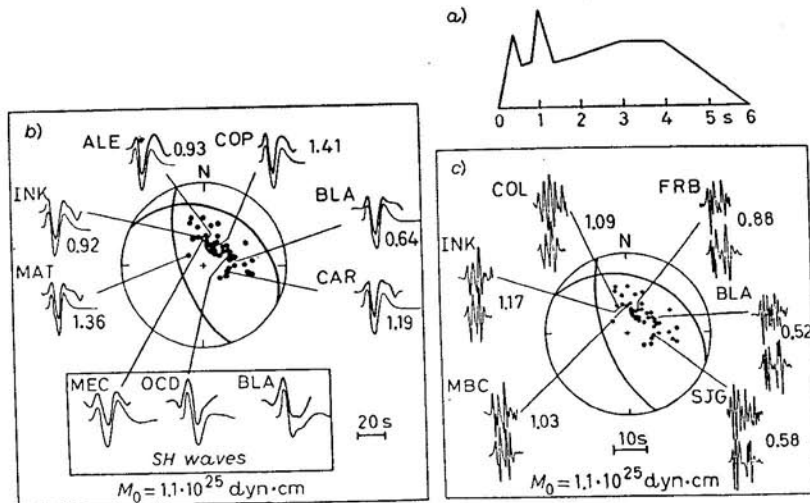


Fig. 5.3. – Modeling experience obtained from studying the near- and far-field records of the 1978 Santa Barbara earthquake: a) displays the far-field time history for an effective point source, b) displays the fit of the long-period synthetics and data, c) displays the short-period fit. (Modified from [32].)

the short periods. Conceptually, we should be able to determine the time structure of the rupture process by simply matching short-period wave form patterns and, indeed, this subject is being pursued vigorously. Unfortunately, at these periods the many idealistic assumptions involving the homogeneity of the mantle, simple flat layering near the source and receivers, planar fault planes, to name a few, begin to break down. Thus the pattern recognition is not so obvious.

A simpler approach is to suppose that the rupture process can be simulated with some small number of point sources where each source has its particular time history. By modeling the long and short periods simultaneously with these few parameters, we can look for substructure. Such a procedure was tried recently by WALLACE *et al.* [32] on the Santa Barbara earthquake of 1978 (see fig. 5.3). These results indicate that on a smaller scale most earthquakes are indeed complex as suggested by KANAMORI and STEWART [46]. The sharp jumps indicated in the time history of fig. 5.3 are obviously important

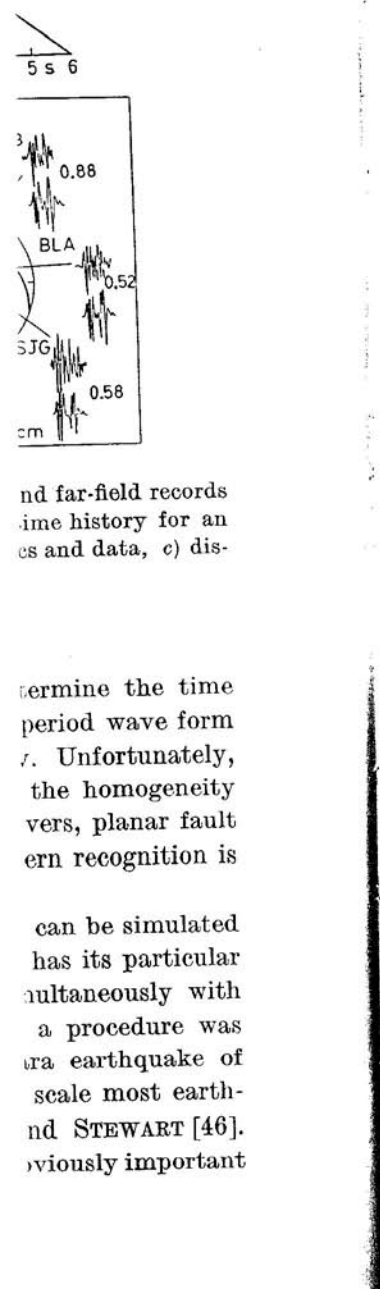
Fig. 5.4. – C where the pre quake, 9.12.1

source orient telesismic v even though difference in

ng (see fig. 5.2).
of the free sur-
; can show con-
l records prove
compared with

with respect to understanding the faulting mechanism, but their existence is particularly significant in estimating earthquake hazards. That is, the high-frequency strong motions appear to be more strongly controlled by the jumps in the time history than by the overall duration (see [32, 42]).

At ranges less than about 30° , we found that the body wave arrivals become multivalued and some care needs to be taken to remove propagational features from source phenomena. Some progress in achieving this separation can be seen in fig. 5.4 and 5.5, where we show that consistent estimates of the



nd far-field records
ime history for an
es and data, c) dis-

termine the time
period wave form
. Unfortunately,
the homogeneity
vers, planar fault
ern recognition is

can be simulated
has its particular
ultaneously with
a procedure was
ra earthquake of
scale most earth-
and STEWART [46].
viously important

Fig. 5.4. — Comparison of synthetics with wave form data at regional distances where the preferred model produces a $\theta = 48^\circ$, $\lambda = 0^\circ$ and $\delta = 79^\circ$, Truckee earthquake, 9.12.1966. (After [47].)

source orientation can be obtained at nearly any range. Note that there are no teleseismic wave forms for the Truckee event compared with the Oroville event, even though they are roughly the same strength. The reason is due to the difference in vertical radiation pattern as discussed earlier (see fig. 3.2). How

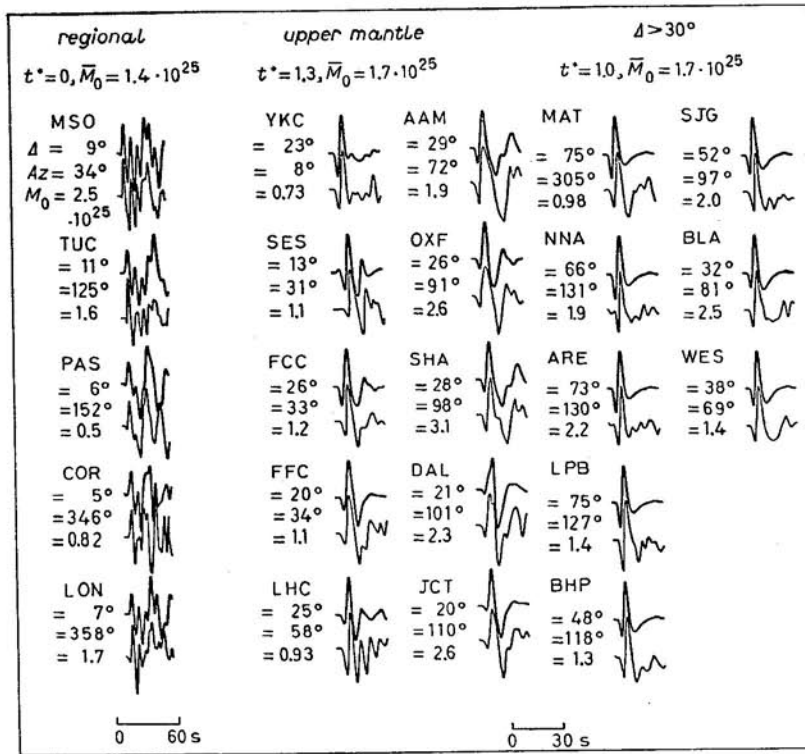


Fig. 5.5. - Comparison of synthetics with wave form data at all ranges with preferred model ($\theta = 215^\circ$, $\lambda = -65^\circ$ and $\delta = 48^\circ$), Oroville earthquake, 8.1.1975. Inversion results: with the 5 P_{nl} records exclusively are $\theta = 195^\circ$, $\lambda = -72^\circ$ and $\delta = 46^\circ$; 10 upper-mantle ranges exclusively are $\theta = 197^\circ$, $\lambda = -63^\circ$ and $\delta = 58^\circ$; 8 teleseismic wave forms exclusively are $\theta = 221^\circ$, $\lambda = -82^\circ$ and $\delta = 44^\circ$. (After [47].)

successful this analysis will be for other regions is not known, but initial results look promising.

* * *

I would like to acknowledge the help of G. ENGEN, J. SAUBER, Z. X. YAO and C. SULENTIC, who have helped assemble this manuscript, and T. WALLACE and J. RIAL for their reviews. I would also like to thank the past and present graduate students who have helped to propel modeling into a respectable field and who have generated many of the figures displayed in this review.

Research supported by the Air Force Office of Scientific Research, ASOFAR Grant No. F49620-01-C-0008. Contribution No. 3790, Division of Geological and Planetary Sciences, California Institute of Technology, Pasadena, Cal. 91125.

APPENDIX

Generalized r.

The method of a seismic record introduced to the reader is understood by

Source	_____
*	_____
h	_____
Th	_____

Fig. A1. - Se

fluid layer p
the asymptotic

$$\bar{\varphi}_1(r, s, z) =$$

$$\bar{\varphi}_2(r, z, s) =$$

$$\bar{\varphi}_3(r, z, s) =$$

with the si
displacemen

These four
Substitutin

APPENDIX

Generalized ray theory.

The method of generalized ray theory allows one to construct the solution of a seismic boundary-value problem by inspection. The method was first introduced to the seismic community by SPENCER [10]. The idea can be easily understood by working through a simple example, namely the sandwiched

Source	Receiver
*	o
h	$\varphi_1, \varrho_1, \alpha_1$
Th	$\varphi_2, \varrho_2, \alpha_2$
	$\varphi_3, \varrho_3, \alpha_3$

Fig. A1. - Schematic of the geometric set-up with a sandwiched fluid layer.

fluid layer problem (see fig. A1). The solution in terms of potentials assuming the asymptotic form becomes

$$\bar{\varphi}_1(r, s, z) = \sqrt{\frac{2}{\pi r s}} \operatorname{Im} \int \frac{\sqrt{p}}{\eta_1} \exp [-s(pr + \eta_1|z-h|)] + A(p) \exp [-s(pr + \eta_1(z+h))] dp ,$$

$$\bar{\varphi}_2(r, z, s) = \sqrt{\frac{2}{\pi r s}} \operatorname{Im} \int \frac{\sqrt{p}}{\eta_1} \exp [-s(pr + \eta_1(z+h))] \cdot [B \exp [-s\eta_2 z] + C \exp [+s\eta_2 z]] dp ,$$

$$\bar{\varphi}_3(r, z, s) = \sqrt{\frac{2}{\pi r s}} \operatorname{Im} \int \frac{\sqrt{p}}{\eta_1} \exp [-s(pr + \eta_1(z+h))] [D(p) \exp [+s\eta_3 z]] dp ,$$

with the simple boundary conditions on continuity of vertical stress and displacement across the interfaces, that is

$$\left. \begin{aligned} \varrho_1 \bar{\varphi}_1 &= \varrho_2 \bar{\varphi}_2 \\ \frac{d\bar{\varphi}_1}{dz} &= \frac{d\bar{\varphi}_2}{dz} \end{aligned} \right\} z = 0 , \quad \left. \begin{aligned} \varrho_2 \bar{\varphi}_2 &= \varrho_3 \bar{\varphi}_3 \\ \frac{d\bar{\varphi}_2}{dz} &= \frac{d\bar{\varphi}_3}{dz} \end{aligned} \right\} z = -Th .$$

These four equations are used to solve for the four unknowns A, B, C and D . Substituting the $\bar{\varphi}_i$ into the boundary conditions, we obtain

$$A = \frac{R_{12} + R_{23} \exp [-2Ths\eta_2]}{1 + R_{12}R_{23} \exp [-2Ths\eta_2]} ,$$

ages with preferred
.1.1975. Inversion
72° and $\delta = 46^\circ$;
58°; 8 teleseismic
fter [47].)

but initial results

UBER, Z. X. YAO
and T. WALLACE
past and present
to a respectable
d in this review.
Research, ASOFR
ion of Geological
, Pasadena, Cal.

where

$$R_{12} = \frac{\varrho_2\eta_1 - \varrho_1\eta_2}{\varrho_2\eta_1 + \varrho_1\eta_2} \quad \text{and} \quad R_{23} = \frac{\varrho_3\eta_2 - \varrho_2\eta_3}{\varrho_3\eta_2 + \varrho_2\eta_3}.$$

Note that, as $Th \rightarrow 0$,

$$A = \frac{\varrho_3\eta_1 - \varrho_1\eta_3}{\varrho_3\eta_1 + \varrho_1\eta_3},$$

and, as $Th \rightarrow \infty$, $A = R_{12}$, as expected.

Next, we use the identity

$$\frac{1}{1+X} = (-1)^n X^n$$

and expand A to obtain a series solution

$$A = R_{12} + \sum_{n=1}^{\infty} (-1)^{n+1} R_{23}^n R_{12}^{n-1} (1 - R_{12}^2) \exp[-2Ths\eta_2 n].$$

Rewriting $\bar{\varphi}_1(r, z, s)$ as

$$\bar{\varphi}_1 = \bar{\varphi}_{\text{direct}} + \bar{\varphi}_{\text{reflected}} + \bar{\varphi}_n,$$

we have

$$\begin{aligned} \bar{\varphi}_n(r, z, s) &= \sqrt{\frac{2}{\pi rs}} \operatorname{Im} \int \frac{\sqrt{p}}{\eta_1} [(-1)^{n+1} R_{23}^n R_{12}^{n-1} (1 - R_{12}^2)] \cdot \\ &\quad \cdot \exp[-s(pr + \eta_1(z + h) - 2Th\eta_2 n)] dp \end{aligned}$$

or

$$\bar{\varphi}_n(r, z, s) = \sqrt{\frac{2}{\pi rs}} \operatorname{Im} \int \frac{\sqrt{p}}{\eta_1} f_n(p) \exp[-s(pr + g_n(p))] dp$$

with

$$f_n(p) = R_{23}^n R_{12}^{n-1} (1 - R_{12}^2) (-1)^{n+1},$$

$$g_n(p) = \eta_1(z + h) + 2Th\eta_2 n.$$

Each value of n corresponds to a particular ray, for example with $n = 1$ we obtain

$$f_1(p) = R_{23}(1 - R_{12}^2)(-1) = T_{12}R_{23}T_{21},$$

$$g_1(p) = 2Th\eta_2 + \eta_1(z + h),$$

where the identity $1 - R_{12}^2 = T_{12}T_{21}$ was used,

$$T_{12} = \frac{2\eta_1\varrho_1}{\varrho_2\eta_1 + \varrho_1\eta_2} \quad \text{and} \quad T_{21} = \frac{2\eta_2\varrho_2}{\varrho_2\eta_1 + \varrho_1\eta_2},$$

Thus the solution is determined by
We can choose
of a sandwich
with the solution

Fig. A2. — 1
20 km source
and $\varrho_3 = 2.4$
amplitudes \pm

and, similarly, for $n = 2$ we obtain

$$f_2(p) = T_{12}R_{23}R_{21}R_{23}T_{21},$$

$$g_2(p) = 4Th\eta_2 + \eta_1(z + h).$$

Thus the solution is built up by adding up the various rays which can be determined by inspection.

We can check our solution and resulting code by generating the step response of a sandwiched layer in the limit of small thickness and compare the results with the solution with no layer (see fig. A2). Next, we examine the case in which

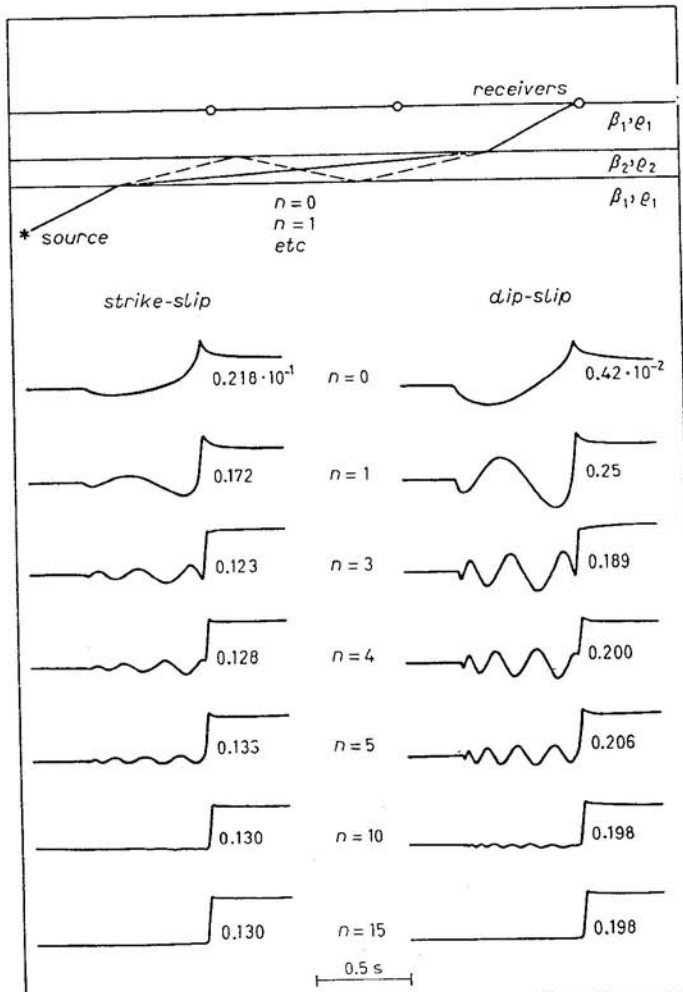


Fig. A2. – Numerical step response of tunneling. The source depth is 3 km with a 20 km source-receiver separation. Seismic parameters are $\rho_1 = 2.3 \text{ g/cm}^3$, $\beta_1 = 2.02 \text{ km/s}$ and $\rho_2 = 2.4 \text{ g/cm}^3$, $\beta_2 = 2.31 \text{ km/s}$, with a barrier thickness of 10 m. Relative peak amplitudes are given for each case. n indicates the number of rays included in the sum.

we go beyond critical angle, so that the receiver is in the geometric shadow, and investigate tunneling. In this case, the layer is too thin to support a head wave and, thus, the strong interference effects introduced by the multiples. The solution can be written

$$\bar{\varphi}_3(r, z, s) = \sqrt{\frac{2}{\pi r s}} \operatorname{Im} \int \frac{\sqrt{p}}{\eta_1} \exp [-s(pr + \eta_1 h + \eta_2 Th + \eta_3 H)] D dp ,$$

where

h = distance from the layer to the receiver,

H = distance from the layer to the source,

Th = layer thickness

and

$$D = T_{12} T_{23} / (1 + R_{12} R_{23} \exp [-2Th\eta_2 s]) .$$

Expanding D in a series yields the ray expansion and the multiples displayed in fig. A2. When the layer is too thin to support head waves, we can obtain a useful approximation by noting that

$$\lim_{Th \rightarrow 0} D = T_{13} = 1 .$$

Thus the only effect of the layer on the solution is in the contour

$$t = pr + \eta_1(h + H) + Th\eta_2 .$$

Essentially, the contour moves off of the real p -axis at $p = 1/\alpha_2$ and, thus, no longer will there be a square-root singularity at the direct arrival time but slightly smoothed depending on the thickness. That is, the height of the steps given in fig. A2 corresponds to the same amplitude of the steps with no layer. However, the rise times of these steps are no longer sharp. Thus, when these step responses are used to generate synthetics, they filter out the high frequencies or short periods. The effect is nearly identical to the Q -operators discussed earlier.

The technique of constructing a solution by simply adding up rays that have traversed the various layers with some specified mode of propagation is called the method of «generalized reflection and transmission coefficients». The coefficients for the solid/solid interface are somewhat more complicated because of the possible mode changes from P to SV , etc., but the procedure is basically the same. The generalized reflection and transmission coefficients used in this paper are given by HELMBERGER [11].

Another concept commonly used in GRT is that of receiver functions. Note that we have been working with potentials throughout these notes. Essentially, we start with a source potential and propagate it to some location by applying the proper product of T and R coefficients. At the receiver we need to convert this potential into a displacement or some measurable quantity. In a whole space, the displacements can be obtained by simply performing the

derivatives def
to displaceme

Fig. A3. – Sch
function: 1) di

satisfy the bo
the three arr
functions ».

where

The second s
radial. The 1

REFE REN

- [1] E. W. C
- [2] W. I. F
- [3] J. B. M
- [4] R. MADA
- [5] N. A. H
- [6] H. LAMI
- [7] E. STRIC
- [8] A. T. D
- [9] L. KNO
- [10] T. SPEN
- [11] D. V. F
- [12] D. G. F
- [13] D. V. F

V. HELMBERGER

metric shadow,
support a head
the multiples.

$H)D dp$,

derivatives defined by eq. (2.24). On a free surface the conversion from potential to displacement becomes more complicated (see fig. A3). The proper way to

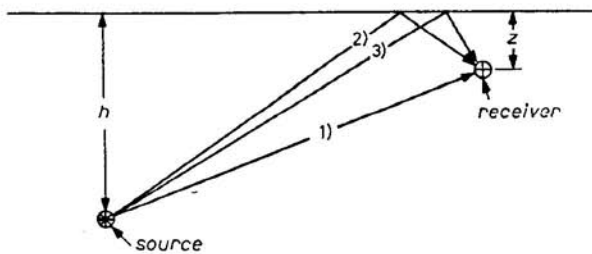


Fig. A3. – Schematic showing the interaction of the three arrivals that form the receiver function: 1) direct P , 2) reflected P , 3) reflected SV .

satisfy the boundary conditions is to take the limit as Z goes to zero and sum the three arrivals since the travel paths coincide and label the results « receiver functions ». The results for incoming P -waves are

$$R_{PZ} = 2\eta_\alpha(\eta_\beta^2 - p^2)/\beta^2 D(p),$$

$$R_{PR} = -4\eta_\alpha\eta_\beta p/\beta^2 D(p),$$

where

$$D(p) = (\eta_\beta^2 - p^2) + 4p^2\eta_\alpha\eta_\beta.$$

The second subscript indicates component, namely Z for vertical and R for radial. The results for incoming SV -waves are

$$R_{SZ} = 4p\eta_\alpha\eta_\beta/\beta^2 D(p),$$

$$R_{SR} = 2\eta_\beta(\eta_\beta^2 - p^2)/\beta^2 D(p).$$

REFERENCES

- [1] E. W. CARPENTER: *Geophysics*, **32**, 17 (1967).
- [2] W. I. FUTTERMAN: *J. Geophys. Res.*, **67**, 5279 (1962).
- [3] J. B. MINSTER: *Geophys. J.*, **52**, 503 (1978).
- [4] R. MADARIAGA: *Bull. Seismol. Soc. Am.*, **66**, 639 (1976).
- [5] N. A. HASKELL: *Bull. Seismol. Soc. Am.*, **54**, 1811 (1964).
- [6] H. LAMB: *Philos. Trans. R. Soc. London Ser. A*, **203**, 1 (1904).
- [7] E. STRICK: *Philos. Trans. R. Soc. London Ser. A*, **251**, 465 (1959).
- [8] A. T. DE HOOP: *Appl. Sci. Res. B*, **8**, 349 (1960).
- [9] L. KNOPOFF and F. GILBERT: *Bull. Seismol. Soc. Am.*, **49**, 163 (1959).
- [10] T. SPENCER: *Geophysics*, **25**, 625 (1960).
- [11] D. V. HELMBERGER: *Bull. Seismol. Soc. Am.*, **58**, 179 (1968).
- [12] D. G. HARKRIDER: *Geophys. J.*, **47**, 97 (1976).
- [13] D. V. HELMBERGER: *Bull. Seismol. Soc. Am.*, **64**, 45 (1974).

- [14] R. BURRIDGE, E. R. LAPWOOD and L. KNOPOFF: *Bull. Seismol. Soc. Am.*, **54**, 1889 (1964).
- [15] F. J. GILBERT and D. V. HELMBERGER: *Geophys. J.*, **27**, 57 (1972).
- [16] D. G. HARKRIDER and D. V. HELMBERGER: *Bull. Seismol. Soc. Am.*, **68**, 125 (1978).
- [17] D. V. HELMBERGER and D. G. HARKRIDER: *Modeling earthquakes with generalized ray theory*, in *Proceedings of IUTAM Symposium: Modern Problems in Elastic Wave Propagation*, edited by J. MIKLOWITZ and J. ACHEENBACK (New York, N.Y., 1978).
- [18] C. A. LANGSTON and D. V. HELMBERGER: *Geophys. J. R. Astron. Soc.*, **42**, 117 (1975).
- [19] T. H. HEATON and D. V. HELMBERGER: *Bull. Seismol. Soc. Am.*, **68**, 31 (1978).
- [20] T. H. HEATON and D. V. HELMBERGER: *Bull. Seismol. Soc. Am.*, **67**, 315 (1977).
- [21] D. V. HELMBERGER and S. D. MALONE: *J. Geophys. Res.*, **80**, 4881 (1975).
- [22] T. L. HONG and D. V. HELMBERGER: *Bull. Seismol. Soc. Am.*, **67**, 995 (1977); **68**, 1313 (1978).
- [23] T. H. HEATON and D. V. HELMBERGER: *Bull. Seismol. Soc. Am.*, **69**, 1311 (1979).
- [24] L. J. BURDICK and G. R. MELLMAN: *Bull. Seismol. Soc. Am.*, **66**, 1485 (1976).
- [25] C. A. LANGSTON and R. BUTLER: *Bull. Seismol. Soc. Am.*, **66**, 1111 (1976).
- [26] G. S. STEWART and D. V. HELMBERGER: *J. Geophys. Res.*, **86**, 7027 (1981).
- [27] C. A. LANGSTON and D. E. BLUM: *Bull. Seismol. Soc. Am.*, **67**, 693 (1977).
- [28] D. V. HELMBERGER and G. R. ENGEN: *Bull. Seismol. Soc. Am.*, **70**, 1699 (1980).
- [29] F. HRON and E. R. KANASEWICH: *Bull. Seismol. Soc. Am.*, **61**, 1169 (1971).
- [30] T. C. WALLACE and D. V. HELMBERGER: *Phys. Earth Planet. Inter.*, **30**, 185 (1982).
- [31] T. C. WALLACE, D. V. HELMBERGER and G. R. MELLMAN: *J. Geophys. Res.*, **86**, 1679 (1981).
- [32] T. C. WALLACE, D. V. HELMBERGER and J. E. EBEL: *Bull. Seismol. Soc. Am.*, **71**, 1701 (1981).
- [33] Y. B. TSAI and K. AKI: *Bull. Seismol. Soc. Am.*, **60**, 1199 (1970).
- [34] L. J. BURDICK: *Broad-band seismic studies of body waves*, Ph. D. Thesis, California Institute of Technology (Pasadena, Cal., 1977).
- [35] D. V. HELMBERGER: *Geophys. J.*, **34**, 251 (1973).
- [36] L. J. BURDICK: *J. Geophys. Res.*, **86**, 5926 (1980).
- [37] L. J. BURDICK and D. V. HELMBERGER: *J. Geophys. Res.*, **83**, 1699 (1978).
- [38] S. P. GRAND and D. V. HELMBERGER: *Geophys. J.*, in press.
- [39] K. E. BULLEN: *An Introduction to the Theory of Seismology*, third edition (Cambridge, 1965), Chapt. VIII.
- [40] L. J. BURDICK and J. A. ORCUTT: *Geophys. J.*, **58**, 261 (1978).
- [41] V. F. CORMIER and G. L. CHOY: *J. Geophys. Res.*, **86**, 1673 (1981).
- [42] J. E. EBEL and D. V. HELMBERGER: *Bull. Seismol. Soc. Am.*, **72**, 413 (1982).
- [43] H. L. LIU and D. V. HELMBERGER: *Bull. Seismol. Soc. Am.*, **73**, 201 (1983).
- [44] C. A. LANGSTON: *Bull. Seismol. Soc. Am.*, **68**, 31 (1978).
- [45] T. H. HEATON: *Bull. Seismol. Soc. Am.*, **72**, 2037 (1982).
- [46] H. KANAMORI and G. S. STEWART: *J. Geophys. Res.*, **83**, 3427 (1978).
- [47] Z. X. YAO, T. C. WALLACE and D. V. HELMBERGER: *Earthqu. Notes*, **53**, 38 (1982).

Strong-Motion

K. AKI

Massachusetts Inst.

1. - Introducti

Strong-motion from large ear seismology. H but at least ea vicinity of a l

Neverthele understanding of an earthqu trolling high-f the opposite f for only two lished by PU earthquakes.

Strong-mo engineering. earthquake e strong motion involved in deterministic their interpre oratory result fault rupture quake ruptu Such a relati for an earthq

The prese seismological, evaluation. C understandin